HAL
open science

Multi-material topology optimization using Wachspress interpolations for designing a 3-phase electrical machine stator

Théodore Cherrière, Luc Laurent, Sami Hlioui, François Louf, Pierre Duysinx, Christophe Geuzaine, Hamid Ben Ahmed, Mohamed Gabsi, Eduardo Fernández

▶ To cite this version:

Théodore Cherrière, Luc Laurent, Sami Hlioui, François Louf, Pierre Duysinx, et al.. Multi-material topology optimization using Wachspress interpolations for designing a 3-phase electrical machine stator. Structural and Multidisciplinary Optimization, 2022, 65 (12), pp.352. 10.1007/s00158-022-03460-1 . hal-03876090

HAL Id: hal-03876090

https://hal.science/hal-03876090v1

Submitted on 5 Dec 2022

HAL is a multi-disciplinary open access archive for the deposit and dissemination of scientific research documents, whether they are published or not. The documents may come from teaching and research institutions in France or abroad, or from public or private research centers.

L'archive ouverte pluridisciplinaire **HAL**, est destinée au dépôt et à la diffusion de documents scientifiques de niveau recherche, publiés ou non, émanant des établissements d'enseignement et de recherche français ou étrangers, des laboratoires publics ou privés.

Multi-material topology optimization using Wachspress interpolations for designing a 3-phase electrical machine stator

Théodore Cherrière[*,a]
Luc Laurent[b,c]
Sami Hlioui[d]
François Louf[e]
Pierre Duysinx[f]
Christophe Geuzaine[g]
Hamid Ben Ahmed[h]
Mohamed Gabsi[a]
Eduardo Fernández[f]

[a] SATIE laboratory, ENS Paris-Saclay, CNRS, Université Paris-Saclay, 91190 Gif-sur-Yvette, France
[b] Laboratoire de Mécanique des Structures et des Systèmes Couplés, EA 3196, Conservatoire national des arts et métiers, F-75003 Paris, France
[c] HESAM University, Paris, France
[d] SATIE Laboratory, CY Cergy Paris University, CNRS, Paris-Saclay University, 95000 Cergy, France
[e] LMPS - Laboratoire de Mécanique Paris-Saclay, Université Paris-Saclay, CentraleSupélec, ENS Paris-Saclay, CNRS, 91190 Gif-sur-Yvette, France
[f] Department of Aerospace and Mechanical Engineering, University of Liège, 4000 Liège, Belgium.
[g] Department of Electrical Engineering and Computer Science, University of Liège, 4000 Liège, Belgium.
[h] SATIE Laboratory, ENS Rennes, CNRS, 35170 Bruz, France
[*] Corresponding author
theodore.cherriere@ens-paris-saclay.fr

Abstract

This work uses Multi-Material Topology Optimization (MMTO) to maximize the average torque of a 3-phase Permanent Magnet Synchronous Machine (PMSM). Eight materials are considered in the stator: air, soft magnetic steel, three electric phases, and their three returns. To address the challenge of designing a 3-phase PMSM stator, a generalized density-based framework is used. The proposed methodology places the prescribed material candidates on the vertices of a convex polytope, interpolates material properties using Wachspress shape functions, and defines Cartesian coordinates inside polytopes as design variables. A rational function is used as penalization to ensure convergence towards meaningful structures, without the use of a filtering process. The influences of different polytopes and penalization parameters are investigated. The results indicate that a hexagonal-based diamond polytope is a better choice than the classical orthogonal domains for this MMTO problem. In addition, the proposed methodology yields high-performance designs for 3-phase PMSM stators by implementing a continuation method on the electric load angle.

Keywords: Density Methods – Electrical Machine – Multimaterial Topology Optimization – Nonlinear Magnetostatics – Wachspress' Shape Functions

- Open Archive HAL with file: hal-03876090
- Doi: 10.1007/s00158-022-03460-1

Contents

1 Introduction **2**

2 Topology optimization framework **4**
2.1 Physical problem . . . 4
2.2 Optimization problem . . . 5
2.3 Optimization algorithm . . . 6

3 Interpolation scheme **9**
3.1 Interpolation domain . . . 9
3.2 Materials placement . . . 10
3.3 Basis functions . . . 10
3.4 Penalization . . . 11

4 Numerical examples and discussion **12**
4.1 Presentation of the problem . . . 12
4.2 Interpolation domain . . . 13
4.3 Penalization parameter . . . 17
4.4 Discussion on the local optima issue . . . 19
4.4.1 Influence of the remanence . . . 20
4.4.2 Influence of the penalization . . . 21
4.4.3 Parametric ψ adjustement . . . 22

5 Conclusion **24**

References **26**

1 Introduction

Since the seminal work of Bendsøe and Kikuchi [1], Topology Optimization (TO) has experienced considerable advances driven by the widespread interest in industry. The achievement owes to the high number of contributions that have improved computational efficiency [2] and expanded its applicability beyond solid mechanics to other physics [3]. Among different TO approaches [4], such as level-set the density method stands out. In the context of structural optimization, each mesh element is associated with a design variable (called density) that takes a value of 0 to represent a void phase or a value of 1 to represent a solid phase. After solving the optimization problem, solid elements define the optimized design. In order to obtain a well-posed problem, design variables are interpolated continuously between 0 and 1. The relaxation also enables sensitivities computation in order to use efficient optimization algorithms such as gradient descent, thanks to the adjoint variable method. To avoid intermediate values in the final design, these are penalized, for instance, by a power-law [5] or a rational function [6]. A substantial extension of density-based methods called Multiple Materials in Topology Optimization (MMTO) appeared with the work of Thomsen [7]. Notably, these methodologies have been widely used in compliance minimization problems that consider isotropic materials with different Young's moduli. Advances in MMTO have spanned different fields involving the design of compliant mechanisms [8], lattice structures [9], thermomechanically constrained porous composites [10], structural joints [11], piezoelectric structures [12], among many others. Other MMTO methodologies include level-set approaches [13, 14], phase field approaches, such as Cahn-Hilliard dynamics [15] or accelerated constrained Allen-Cahn

dynamics [16, 17]. Recently, Chandrasekhar and Suresh [18] used neural networks to represent the volume fraction of different materials.

In the magnetostatics field, MMTO emerged with the work of Dyck and Lowther [19]. The authors optimized a magnetic bearing, composed of steel, air and conductors, by interpolating each physical property (magnetic permeability and current density). They also eliminated intermediate materials with penalization. Concerning density methods, the most common applications are C-core electromagnets as in Wang, Park, and Kang [20] and Wang et al. [21], which contain steel, air and a source – current density, Permanent Magnets (PM) or both. The application on which the highest number of materials are used is the design of Halbach arrays, where different PMs are distributed to maximize the flux density. This problem was tackled in 3D [22] and with arbitrary PM directions [23], which were included within the optimization variables. Steel was added in the optimization to design moving actuators. Lee, Dede, and Nomura [24] placed several materials to maximize the force profile of a plunger. This work was extended in Lee et al. [25] to include more PMs and in Jung, Lee, and Lee [26] to produce manufacturable structures.

Concerning MMTO applied to electrical machines, many works use heuristic approaches as in Sato, Watanabe, and Igarashi [27] and Jung, Ro, and Jung [28], mainly to optimize only the rotor of electrical machines. Density-based methodologies are also used to optimize rotors of different kinds of actuators, such as wound field synchronous machines [29], permanent magnet synchronous reluctance motors [30, 31], or permanent magnet synchronous machines [32], and can be hybridized with shape optimization [33]. By contrast, very few works tackle the stator optimization. Among them, Lee, Seo, and Kikuchi [34] and Choi et al. [35] optimize the stator teeth without changing the conductor distribution, and Labbé and Dehez [36] includes only one phase of a reluctant machine within the optimization.

In order to consider many materials, the traditional density method can be extended. One solution is to interpolate M materials using $M-1$ auxiliary variables per mesh element [37]. Other methods require a single variable per element by using peak functions [38], or by ordering several interpolation functions in ascending order [39]. Authors have proposed the use of M optimization variables (one per candidate layer) in a scheme denoted as Discrete Material Optimization [DMO, see 40]. More recently, Bruyneel [41] proposed placing candidate materials at the vertices of a rectangular domain. The design variable is a point inside the domain that interpolates material properties. Thus, $M = 4$ candidate materials can be handled using two design variables: the Cartesian coordinates of the inner point. This idea, denoted as Shape Function with Penalization (SFP), was then extended to handle $M = 8$ candidate materials using hexahedral domains and three design variables per element [42, 43] and has been successfully applied, mainly in the design of fiber-reinforced composites [44].

The literature proposes two possibilities to handle a different number of materials. The majority of works use redundant materials (mostly air) as Sigmund [45] to fill the vertices of an orthogonal interpolation domain. However, no element indicates that orthogonal domains suit all MMTO problems. Jung and Min [46] have shown that the attribution of these redundant materials may affect the optimization results. A comparison of two different materials placements is given in Fig. 1a and Fig. 1b. Other authors, as Choi and Yoo [47] use linear programming to handle a linear constraint per mesh element, as illustrated in Fig. 1c. As the obtained triangular domain is not equilateral as in Fig. 1d, a permutation of the materials' positions changes the optimization problem.

As an alternative, this paper presents a new method for MMTO based on SFP formalism, using polytopes as catalog domains that allow the inclusion of any number of candidate materials without repeating any of them. To interpolate material properties inside the polytope, we use generalized basis functions [48]. Since the proposed method uses non-orthogonal domains, many linear constraints are required to keep the design variables within the polytope. However, since we consider low-dimensional polytopes, we observe that a straightforward Projecting Gradient Descent (PGD) algorithm is enough to tackle the 3-phase stator design problem.

The structure of this article is organized as follows. Section 2 presents the adopted topology optimization approach, the optimization problem to be solved, and the implemented algorithm. Section 3 details the novelties of this work related to the polytope domains for placing material candidates and the Wachspress functions for interpolating material properties. Section 4 presents design results for the stator of a Permanent Magnet Synchronous Machine (PMSM). Finally, conclusions and perspectives are

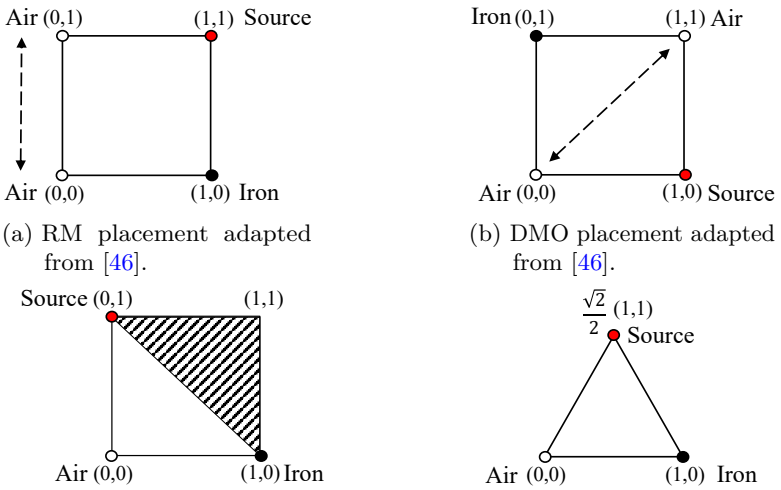

(a) RM placement adapted from [46].

(b) DMO placement adapted from [46].

(c) Adapted from [47].

(d) Other placement (not in the literature).

Figure 1: Different possible materials placements for a C-core electromagnet optimization.

given in Section 5.

2 Topology optimization framework

2.1 Physical problem

Among the wide variety of electromechanical actuators, the 3-phase PMSM is one of the most popular in industrial applications, especially in electrical mobility. It comprises two parts separated by an airgap: a rotating element – the rotor – which contains one or several Permanent Magnets (PM), and a fixed part – the stator – which creates a rotating magnetic field generated by varying electric currents inside coils. For standard electric frequencies, the distribution of the magnetic flux density can be described by magnetostatics, which comes from Maxwell's equations:

$$\nabla \times (\nu(|\boldsymbol{b}|).\nabla \times \mathbf{a}) = \mathbf{j} + \nabla \times \mathbf{m}, \tag{1}$$

where $\mathbf{a} = [a_x \quad a_y \quad a_z]^T$ is the vector potential ensuring the divergence-free of flux density $\boldsymbol{b} = \nabla \times \mathbf{a}$, ν is the magnetic reluctivity, $\mathbf{j} = [j_x \quad j_y \quad j_z]^T$ is the current density, and $\mathbf{m} = [m_x \quad m_y \quad m_z]^T$ is the PM magnetization. Note that ν depends on $|\boldsymbol{b}|$ in the ferromagnetic materials, as shown in Fig. 2. In a 2D problem within the plane (x, y), the x and y components of $\mathbf{a}$ and $\mathbf{j}$ vanish, as well as the z component of $\mathbf{m}$.

Thus, the magnetostatics equation in 2D becomes:

$$\nabla.[\nu(|\boldsymbol{b}|)\nabla a_z] = j_z + \nabla \left(R_{\frac{-\pi}{2}} \boldsymbol{m}_{xy} \right), \tag{2}$$

with $R_{\frac{-\pi}{2}} = \begin{bmatrix} 0 & 1 \\ -1 & 0 \end{bmatrix}$ a rotation operator and $\mathbf{m}_{xy} = [m_x \quad m_y]^T$. The 2D flux density reads:

$$\boldsymbol{b} = R_{\frac{-\pi}{2}} \nabla a_z. \tag{3}$$

Equation (2) can be discretized using, for instance, the Finite Element Method (FEM), which gives the resulting non-linear system:

$$\mathbf{K}(\nu(\boldsymbol{a}))\boldsymbol{a} = \boldsymbol{s}_j(\boldsymbol{j}) + \boldsymbol{s}_m(\boldsymbol{m}), \tag{4}$$

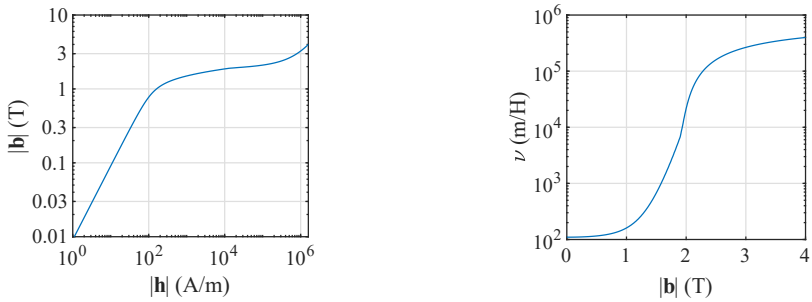

(a) BH curve of FeSi. (b) Reluctivity of FeSi.

Figure 2: FeSi anhysteretic behavior: $\mathbf{h}$ is the magnetic field, $\mathbf{b}$ the flux density and $\nu = \frac{|\mathbf{h}|}{|\mathbf{b}|}$ the reluctivity.

where $\boldsymbol{a}$, $\boldsymbol{j}$ and $\boldsymbol{m}$, are the discretized a_z, j_z and $\mathbf{m}_{xy}$, respectively. $\mathbf{K}$ is the stiffness matrix, $\boldsymbol{a}$ the degrees of freedom, $\boldsymbol{s}_j$ and $\boldsymbol{s}_m$ compose the right-hand side, representing the discretized source terms of the system.

The interaction between PM and stator magnetic fluxes creates a torque T. A formula to compute the torque of 2D rotating machines using spatial integration of Maxwell stress tensor was proposed by Arkkio [49]. It can be written as:

$$T = \left[\frac{2\pi L}{S_{\text{airgap}}} \iint_{\text{airgap}} \boldsymbol{x} \times (\boldsymbol{x}) \, \mathrm{d}s \right] \cdot \boldsymbol{e}_z, \tag{5}$$

where L is the axial length of the machine, S_{airgap} the surface of the airgap between the stator and the rotor, $\boldsymbol{x}$ the position of the integration point, $\boldsymbol{e}_z$ the axial unitary vector, and the magnetic part of the Maxwell stress tensor, which depends on the flux density $\boldsymbol{b}$:

$$\Sigma_{ij} = \nu_0 \left(b_i b_j - \frac{|\boldsymbol{b}|}{2} \delta_{ij} \right). \tag{6}$$

2.2 Optimization problem

This work adopts the density approach. Namely, the design domain is discretized into N triangular finite elements, and the material properties of each element are defined by interpolating the properties of prescribed materials with n design variables. Since multiple materials are considered for the optimization problem and handled in an SFP approach, n depends on the total number of finite elements (N) and the dimension of the interpolation domain. By contrast with the original SFP scheme, the interpolation domain is not limited to orthogonal ones and can be any convex polytope. From now on, this polytope is denoted by $\mathcal{D}$ for the sake of simplicity. To keep a general notation, we define $\mathbf{x}^e$ by the vector containing the n design variables assigned to the mesh element e. That is, $\mathbf{x}^e = [\mathrm{x}_1^e \quad \mathrm{x}_2^e \ \dots \ \mathrm{x}_{\dim(\mathcal{D})}^e]$, where x_i^e denotes the i-Cartesian coordinate inside the polytope associated with the e-element, as shown in Fig. 3. In this work, only 2D and 3D polytopes are considered: $\dim(\mathcal{D}) = 2$ or 3.

The proposed methodology for MMTO is presented for designing a PMSM stator. The objective is to maximize the average torque given by Equation (5), considering multiple materials in the stator with different magnetic reluctivities and current densities, detailed in Section 4. The design problem is formulated as follows:

$$\begin{aligned} \min \quad & f(\mathbf{x}) = -\langle \, T(\boldsymbol{a}(\mathbf{x})) \, \rangle \\ \text{s.t.:} \quad & \mathbf{x}^e \in \mathcal{D} \ , \quad e = 1, \dots, N \\ & \mathbf{K}(\nu(\boldsymbol{a}, \mathbf{x}))\boldsymbol{a} = \boldsymbol{s}_j(\boldsymbol{j}(\mathbf{x})) + \boldsymbol{s}_m(\boldsymbol{m}) \end{aligned} \tag{7}$$

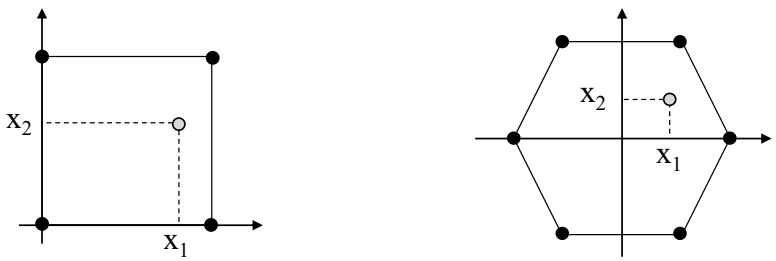

(a) Orthogonal domain (b) Non-orthogonal domain

Figure 3: Examples of interpolation domains. Black dots represent prescribed materials, gray dots represent interpolated materials.

with $\mathbf{x}$ the set of all optimization variables, *i.e.* $\mathbf{x} = [\mathbf{x}^e]_{e\in[\![1,N]\!]}$. Usually, a volume constraint is necessary to avoid the trivial solution, such as a fully solid beam in the compliance minimization problem. However, a fully solid stator cannot produce torque in the case of electrical machines, so a volume constraint is unnecessary and was not used. Moreover, global constraints are non-trivial to implement in the presented approach and thus will be tackled in future works.

2.3 Optimization algorithm

The optimization problem (7) is solved with a Projected Gradient Descent (PGD). The iterative optimization process consists of four steps illustrated in Fig. 4.

The first step is to evaluate the material properties within each finite element from the optimization variables. This procedure will be detailed in Section 3 as it presents the main novelty of this work. The second step is to solve Equation (4) to evaluate the magnetic performance as defined previously (Section 2.1). The third step is to compute the sensitivities using the Adjoint Variable Method (AVM). To do so, the following adjoint problem must be solved [50]:

$$\left(\frac{\partial(\mathbf{K}\boldsymbol{a} - \boldsymbol{s_j} - \boldsymbol{s_m})}{\partial \boldsymbol{a}}\right)^T \boldsymbol{\lambda} = \frac{\partial f}{\partial \boldsymbol{a}}, \tag{8}$$

then the sensitivities to each component i of $\mathbf{x}^e$ are computed for each element e with:

$$\frac{\mathrm{d}f}{\mathrm{d}\mathrm{x}_i^e} = \frac{\partial f}{\partial \mathrm{x}_i^e} + \boldsymbol{\lambda}^T \left(\frac{\partial \boldsymbol{s_j}}{\partial \mathrm{x}_i^e} - \frac{\partial \mathbf{K}}{\partial \mathrm{x}_i^e}\boldsymbol{a}\right). \tag{9}$$

Our implementation of the AVM has been validated by comparison with finite differences. The fourth step of the optimization process is to update the design variables using the Projected Gradient Descent (PGD) algorithm. This algorithm consists of three phases, which are detailed below:

1. **Compute the descent direction**. As sensitivities magnitudes can be very different from one mesh element to another, which leads to slow convergence, each component i of the local descent direction vectors $\boldsymbol{d}^e = [d_1^e \quad d_2^e \ \dots \ d_{\dim(\mathcal{D})}^e]$ associated with a finite element e are normalized as follows:

$$d_i^e = -\frac{\dfrac{\mathrm{d}f}{\mathrm{d}\mathrm{x}_i^e}}{\left\|\dfrac{\mathrm{d}f}{\mathrm{d}\mathbf{x}^e}\right\|}. \tag{10}$$

2. **Estimate the appropriate step size**. The step size at iteration k is denoted as α_k and is adjusted by a simplified trust-region algorithm inspired from Nocedal and Wright [51]. The step

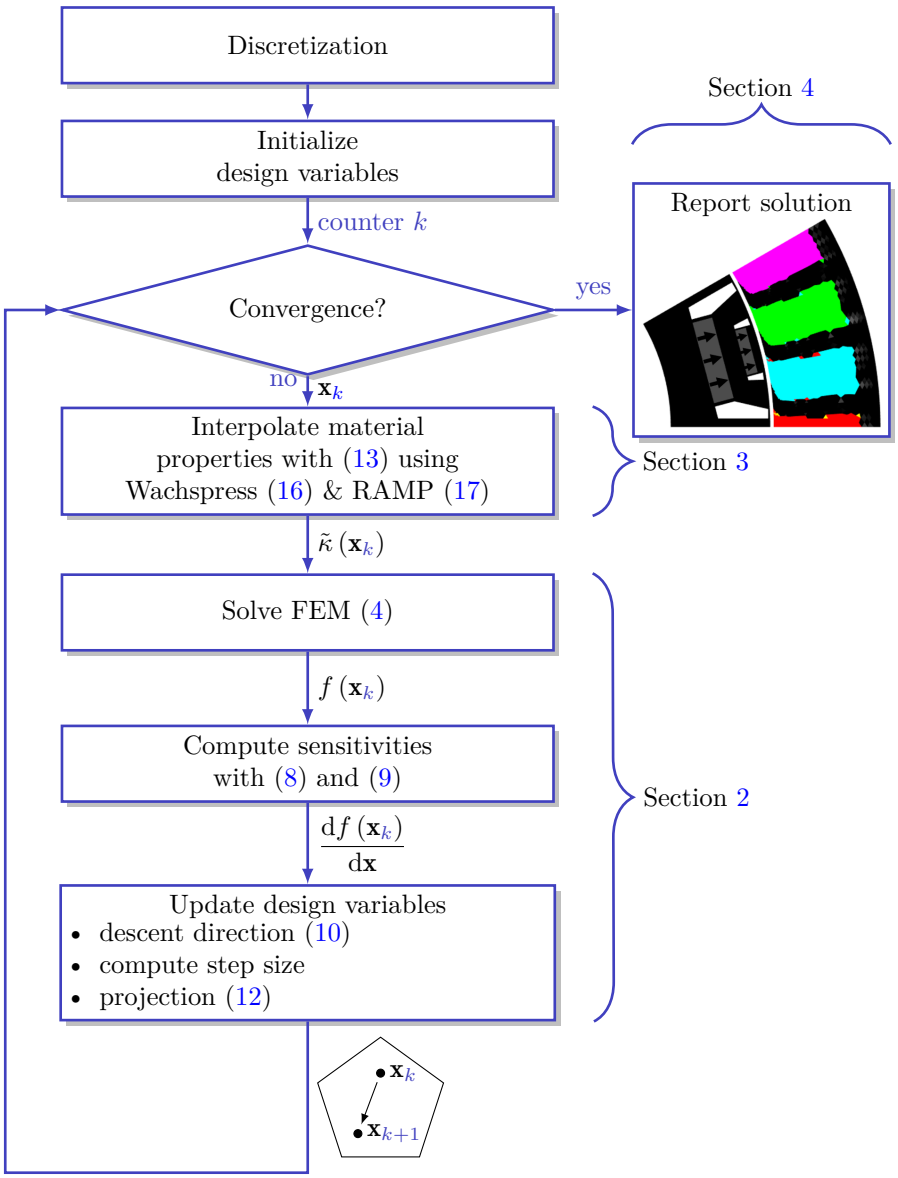

Figure 4: Flowchart of the optimization algorithm.

is heuristically adapted according to the quality of the linearized model. A quality indicator q is defined as:

$$q = \frac{f(\mathbf{x}_k) - f(\mathbf{x}_{k-1})}{\left(\frac{\mathrm{d}f}{\mathrm{d}\mathbf{x}}\right)^T (\mathbf{x}_k - \mathbf{x}_{k-1})}. \tag{11}$$

If the linearized model is considered as bad (when q is too low), the iteration is rejected and the step size is reduced. If the model is considered good enough, the step size is increased to accelerate the convergence. Algorithm 1 details the whole procedure. The initial step size α_0 is set to 0.1.

3. **Projection**. After applying the descent, some points may lie outside the polytope domain $\mathcal{D}$. In that case, they should be projected back onto it using the min-norm operator denoted as $\mathcal{P}$. The PGD update reads:

$$\mathbf{x}_{k+1} = \mathcal{P}(\mathbf{x}_k + \alpha_k \boldsymbol{d}_k). \tag{12}$$

Algorithm 1 Control of the step size α

```
Compute q
if q < 5 × 10^-3 then                                  ▷ The linear model is bad.
    Reject the iteration
    α ⇐ α/2                                            ▷ The step size is decreased.
else if q ∈ [5 × 10^-3, 5 × 10^-2] then
    Accept the iteration
else if q > 5 × 10^-2 then                             ▷ The linear model is good.
    Accept the iteration
    α ⇐ 1.2α                                           ▷ The step size is increased.
end if
Continue the optimization process
```

For orthogonal domains as in Fig. 3a, the application of $\mathcal{P}$ is a simple truncation of $\mathbf{x}$-components. For other types of interpolation domains, it implies considering many linear constraints and finding the active one to project the point onto, which can be a facet, an edge, or a vertex of the polytope. This task can demand an extensive computation time on high-dimensional polytopes without efficient projection algorithms (Haddock 2018). Fortunately, in the present case, $\mathcal{P}$ can be decomposed in N projections of $\mathbf{x}^e$ onto a low dimensional convex polytope $\mathcal{D}$ (2D or 3D). If $\mathbf{x}^e$ is located outside $\mathcal{D}$, it belongs to the normal cone associated with the face i, onto which $\mathbf{x}^e$ should be projected, as shown in Fig. 5.

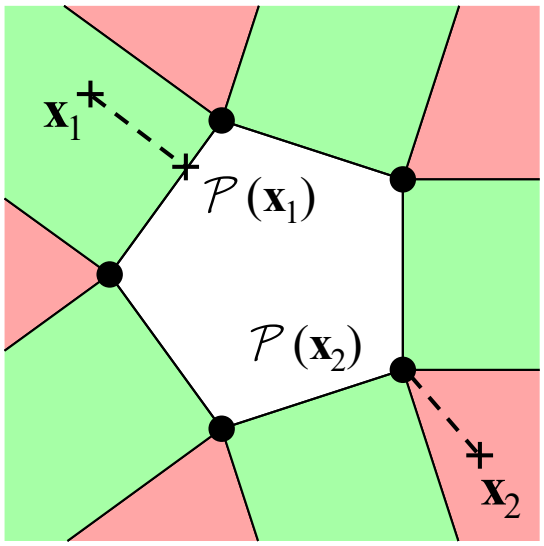

Figure 5: Min-norm projection onto a pentagon: $\mathbf{x}_1$ is associated to an edge and $\mathbf{x}_2$ to a vertex.

It follows a simple procedure to compute $\mathcal{P}(\mathbf{x}^e)$:

a) Compute the *normal fan* of the polytope – defined as the collection of all the normal cones from each of its faces, as shown in Fig. 6. This needs to be done once, at the beginning of the optimization process.

b) Find the normal cone where $\mathbf{x}^e$ is located. The closest face is associated with this cone. It requires testing each cone.

c) Project the point $\mathbf{x}^e$ onto the closest face with the standard orthogonal projector.

A vectorized Matlab 2020b implementation of the projection algorithm is available on Github and archived in Zenodo [52].

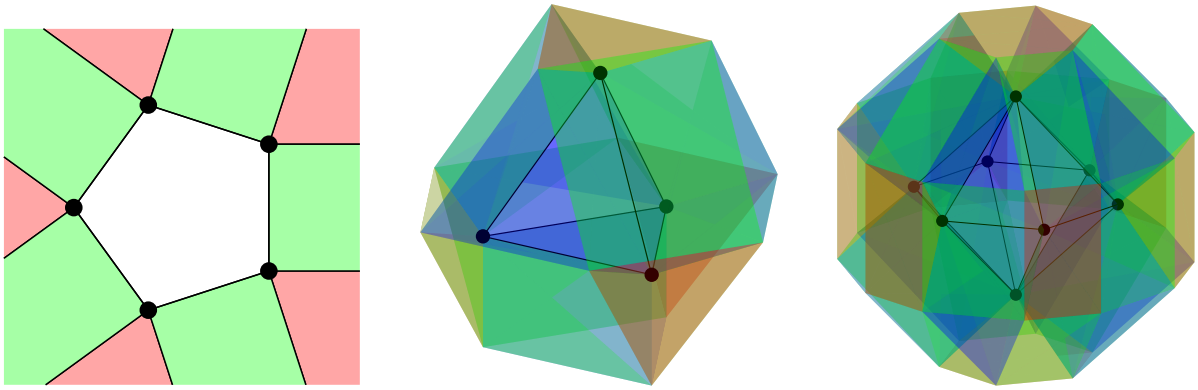

(a) Pentagon (b) Tetrahedron (c) Diamond

Figure 6: Normal fans of different polytopes. Red cones are associated with vertices, green cones with edges and blue cones with facets.

3 Interpolation scheme

The expressions of the interpolated material properties are essential in density-based methods to obtain realistic design solutions. This work proposes to extend the SFP formalism introduced by Bruyneel [41] to a broader class of interpolation domains. In order to build such interpolations, four choices have to be made:

1. The interpolation domain $\mathcal{D}$ with M vertices.
2. The materials placement on its vertices.
3. The basis functions set $\{\omega_v^{\mathcal{D}}\}_{v\in[\![1,M]\!]}$. Each basis function is associated with a vertex v of $\mathcal{D}$.
4. The penalization function P.

After that, the material property $\tilde{\kappa}^e$ of a mesh element e filled with an intermediate material can be constructed from the properties of the prescribed materials κ_v, which possibly depends on the local flux density $\boldsymbol{b}^e$:

$$\tilde{\kappa}^e(\mathbf{x}^e, \boldsymbol{b}^e) = \sum_{v=1}^{M} \kappa_v(|\boldsymbol{b}^e|) \cdot P(\omega_v^{\mathcal{D}}(\mathbf{x}^e)). \tag{13}$$

Note that it is possible to associate a different penalization function for each vertex. However, we consider the same penalization function P for every vertex for simplicity. The derivative of (13) with respect to the i-component of $\mathbf{x}^e$ is necessary to compute the sensitivities with (9), and reads:

$$\frac{\mathrm{d}\tilde{\kappa}^e}{\mathrm{d}\mathrm{x}_i^e}(\mathbf{x}^e, |\boldsymbol{b}^e|) = \sum_{v=1}^{M} \kappa_v(|\boldsymbol{b}^e|) P'(\omega_v^{\mathcal{D}}(\mathbf{x}^e)) \frac{\mathrm{d}\omega_v^{\mathcal{D}}(\mathbf{x}^e)}{\mathrm{d}\mathrm{x}_i^e}. \tag{14}$$

3.1 Interpolation domain

The first step consists in choosing a suitable domain $\mathcal{D}$ for the material interpolation, with each prescribed material associated with one of its vertices. In the literature, only hypercubes of $[0,1]^{\dim}$ are chosen. Hypercubes are orthogonal domains that can contain $2^{\dim}$ materials. Their main advantage is their boundary constraints, which can be easily handled by a simple truncation algorithm. However, compared to other polytopes, hypercubes may not be suitable for some MMTO problems because, as shown in our numerical examples (Section 4), they promote local optima even when the number of prescribed materials is a power of two. This work considers 2D and 3D convex polytopes as admissible domains. Some examples are presented in Table 1.

	$\dim(\mathcal{D}) = 2$	$\dim(\mathcal{D}) = 3$
Hyper-cubes (current state of the art)	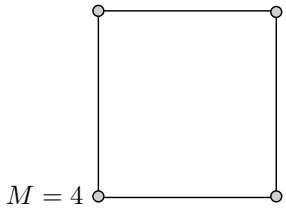	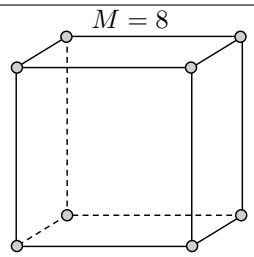
Other possible convex polytopes	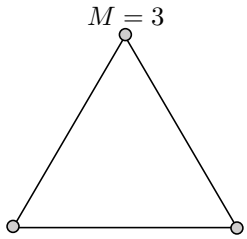 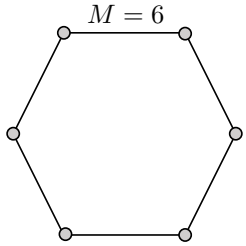	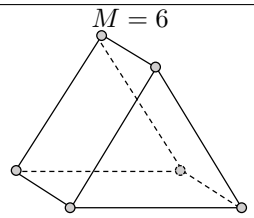 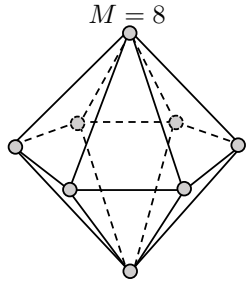
Forbidden domains	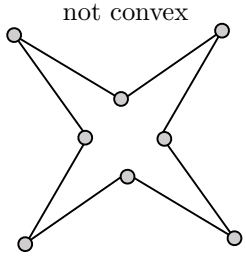	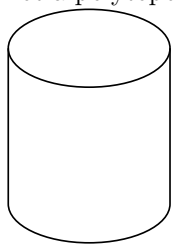

Table 1: Examples of admissible interpolation domains.

3.2 Materials placement

The next step consists of associating each material considered in the optimization to a vertex of $\mathcal{D}$.

As shown by [46], the results of the optimization depend on the materials placement. An intuitive choice for the 3-phase PMSM stator optimization problem is to place the electric sources on the same plane, according to their phases, in orthogonality with steel. This can be made with a hexagonal-based diamond but not with a classical orthogonal domain such as a cube. The methodology presented in this paper can efficiently handle any convex polytope, which is essential for complex MMTO problems such as a 3-phase PMSM stator optimization as shown by our numerical experiments (Section 4.2).

3.3 Basis functions

Once the domain $\mathcal{D}$ and the materials placement are chosen, an interpolation can be defined thanks to a set of differentiable basis functions $\omega_v^{\mathcal{D}} : \mathcal{D} \to [0, 1]$ associated with each vertex v, such as $\omega_v^{\mathcal{D}} = 1$ on the vertex v and 0 on the others. An interesting property is the partition of unity:

$$\forall \mathbf{x}^e \in \mathcal{D}, \quad \sum_{v=1}^{M} \omega_v^{\mathcal{D}}(\mathbf{x}^e) = 1, \tag{15}$$

which allows the interpretation the basis functions as material volume fractions. However, partition of unity is required only at the end of the optimization process, so the penalization of the intermediate values of the basis functions is possible [41] and will be detailed in Section 3.4. Several different basis functions meet the partition of unity, such as Wachspress, mean-value, or Malsch interpolant, see Sukumar and Malsch [53] and Kraus, Rajagopal, and Steinmann [54]. In this paper, we use [48] basis functions, which read in 2D:

$$\begin{aligned} \omega_v(\mathbf{x}^e) &= \frac{\varphi_v(\mathbf{x}^e)}{\sum_{j=1}^{M} \varphi_j(\mathbf{x}^e)}, \\ \text{with} \qquad \varphi_v(\mathbf{x}^e) &= \frac{A_v}{A_v^+(\mathbf{x}^e).A_v^-(\mathbf{x}^e)}, \end{aligned} \tag{16}$$

where $A_v^-(\mathbf{x}^e)$, $A_v^+(\mathbf{x}^e)$, A_v represent the areas of the triangles defined, respectively, by vertices $[\mathbf{x}_{v-1}^e, \mathbf{x}_v^e, \mathbf{x}^e]$, $[\mathbf{x}_v^e, \mathbf{x}_{v+1}^e, \mathbf{x}^e]$ and $[\mathbf{x}_{v-1}^e, \mathbf{x}_v^e, \mathbf{x}_{v+1}^e]$ as shown in Fig. 7a. An example of basis function is plotted in Fig. 7b. In higher dimensions, A_v becomes a simplex hypervolume related to the adjacent facets. A code to compute the basis functions values as well as their gradients for any convex 2D and 3D polytopes is given by Floater, Gillette, and Sukumar [55]. A vectorized version of this code was used to handle many points [52].

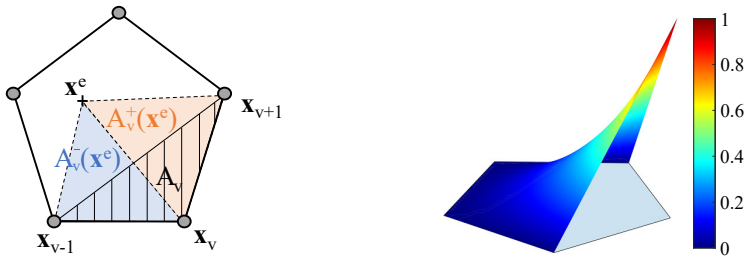

(a) Construction of a Wachspress basis function.

(b) Values of a Wachspress basis function.

Figure 7: Illustration of a Wachspress basis function associated with a vertex of a pentagon.

3.4 Penalization

An interpolation built with basis functions matching the partition of unity may not lead to meaningful designs. Some intermediate materials often remain, and a penalization P is necessary to avoid them. A wide variety of such functions exists. The most popular is the power-law from the SIMP method [5]. In this paper, we chose to use the RAMP [6] applied to each basis function:

$$P : \begin{cases} [0,1] \to [0,1] \\ \omega \mapsto \dfrac{\omega}{1 + p(1-\omega)} \end{cases}, \tag{17}$$

where p is the penalization factor. The RAMP was preferred to the classical SIMP scheme because it preserves the non-zero gradient of the basis functions on all the vertices of the polytope, as shown in Fig. 8.

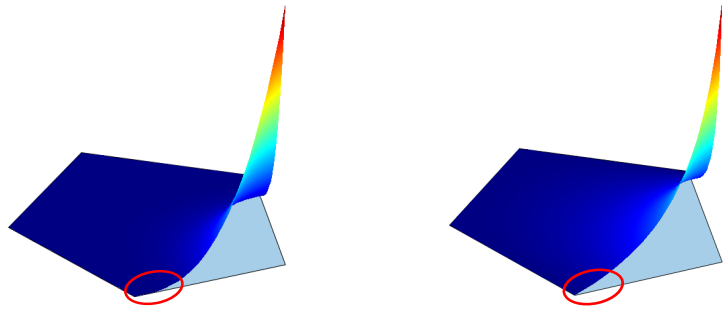

(a) SIMP - $p = 3$. The gradient is zero in the circled zone.

(b) RAMP (17) - $p = 4$. The gradient does not vanish anywhere.

Figure 8: Examples of penalized Wachspress functions.

4 Numerical examples and discussion

The presented methodology can handle numerous materials. As an example, we applied it to the MMTO of a complete three-phase PMSM stator. Although three-phase machines are widely used in industrial applications, only their rotor is generally optimized as in Sato and Igarashi [56], and sometimes with the stator teeth [34, 35]. When the magnetic source distribution has been addressed, only one electric phase had been considered, as in Labbé and Dehez [36]. This numerical example is the MMTO of a 3-phase PMSM, containing all electrical phases, steel, and air. To the authors' knowledge, this problem has not been addressed in the literature, perhaps because of the high number of materials and the lack of appropriate interpolation domains.

4.1 Presentation of the problem

We consider Equation (7) as the optimization problem. It contains $M = 8$ materials to distribute within the stator, summarized in Table 2:

- Air, which is a linear material with a magnetic reluctivity of $\nu_0 = \dfrac{1}{4\pi \times 10^{-7}}$m/H.
- Steel, which has a non-linear behavior. Its reluctivity is given in Fig. 2b and follows the anhysteretic behavior of standard FeSi.
- Six different types of copper conductors, which have the same magnetic behavior as air. They carry current densities j_α with the same amplitude but different electrical phases:

$$j_\alpha(\theta_e) = J\cos(p_p\theta - \alpha\pi/3 + \psi_{\text{optim}}), \alpha \in [\![0, 5]\!] \tag{18}$$

  where J is the amplitude of the current density set to $10\,\text{A/mm}^2$, θ is the mechanical angle varying from $0°$ to $30°$, $p_p = 6$ is the number of poles pairs, and ψ_{optim} is the fixed load angle set to $288°$, which corresponds to the load angle where the torque is maximum on the reference design in Fig. 9.

The load angle ψ can be interpreted as either a magnetic rotation of the magnetic fields created from the stator without mechanical rotation or a mechanical rotation of the stator without magnetic rotation, as shown in Fig. 10.

The torque is computed with (5) on 60 angular positions of the rotor and averaged. The rotor is inspired by the one of the BMW i3 [57] shown in Fig. 9. The problem is discretized on a mesh generated with Gmsh [58] shown in Fig. 11. As the rotor structure is periodic, only one magnetic pole is considered in the FEM analysis. Therefore, only this pole of the obtained designs will be shown to save space in the rest of the article.

Table 2: Materials used in the optimization

Material	Reluctivity	Current density
Air	ν_0	0
Steel (FeSi)	$\nu(\lvert\boldsymbol{b}\rvert)$ – see Fig. 2b	0
Phase A^+	ν_0	$J\cos(\theta_e+\psi)$
Phase A^-	ν_0	$J\cos(\theta_e-\pi+\psi)$
Phase B^+	ν_0	$J\cos(\theta_e-2\pi/3+\psi)$
Phase B^-	ν_0	$J\cos(\theta_e-5\pi/3+\psi)$
Phase C^+	ν_0	$J\cos(\theta_e-4\pi/3+\psi)$
Phase C^-	ν_0	$J\cos(\theta_e-\pi/3+\psi)$

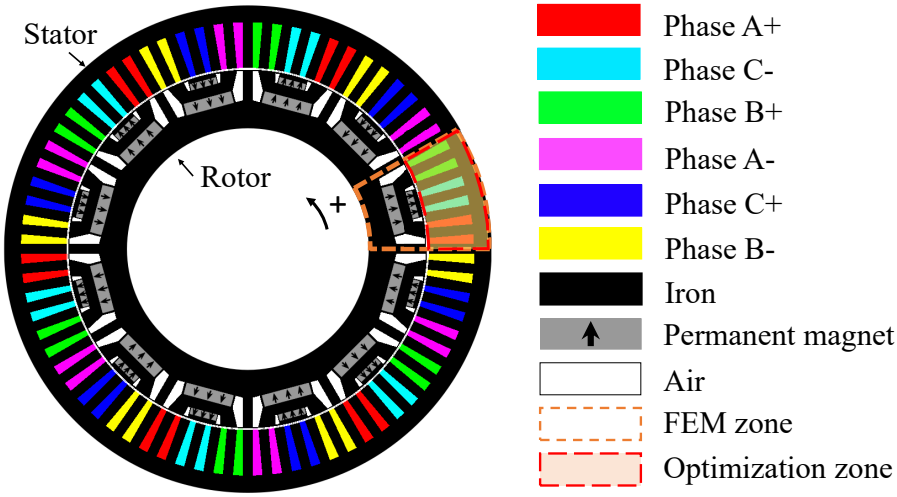

Figure 9: Reference design adapted from the BMW i3 [57].

The numerical examples are used to assess three main aspects of the proposed methodology: (i) the polytope domain $\mathcal{D}$, (ii) the penalization parameter p, and (iii) the load angle ψ. In the following section, the first aspect is discussed.

4.2 Interpolation domain

The choice of the interpolation domain is essential and beyond the number of materials M. Indeed, it exists several possible polytopes which have M vertices. Since this work considers eight candidate materials, it is interesting to compare the performance of the proposed MMTO approach using different 8-vertex polytopes. The polytopes under analysis are a 2D octagon (Fig. 12a), a 3D cube (Fig. 12b) and a 3D diamond (Fig. 12c). The 3D cube is representative of the literature [42], but the octagon and the diamond are new domains in MMTO, to the best of our knowledge.

We place the conductors consistently with their electric phases, which is easy for the diamond domain, but not for the others. At the beginning of the optimization process, the design variables are placed at the centroid of the polytopes. All the other optimization parameters are strictly the same. The material properties ν and j are interpolated by using Equation (17), with $p_\nu = 4$ and $p_j = 3$. These penalization values are justified in Section 4.3. The PGD was applied during 500 iterations, and the final structures are plotted in Fig. 12.

We note that no design contains air, which is logical because air has the same magnetic behavior as conductors but carries no current. Therefore, they cannot increase the torque more than conductors. Visually, the best-defined design is given by the diamond domain in Fig. 12c. For that design, the

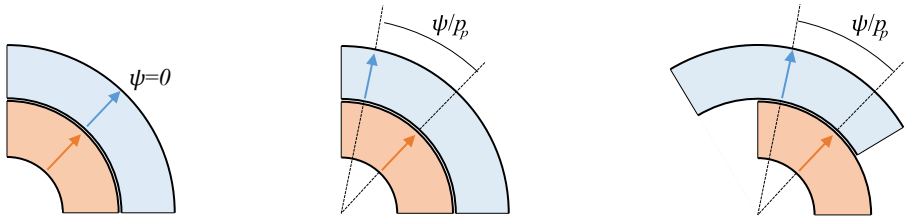

(a) Reference mechanical and magnetic angles.

(b) ψ seen as a magnetic angle.

(c) ψ seen as a mechanical angle.

Figure 10: Equivalence between load angle ψ interpretations. Arrows represent magnetic field reference. The rotor is represented in orange and the stator in blue.

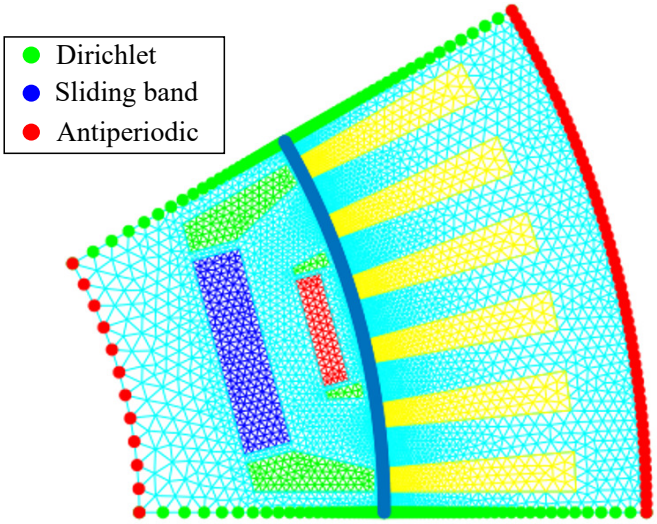

Figure 11: Mesh with boundary conditions obtained (11331 triangles, 5890 nodes).

optimized design variables are displayed in Fig. 13 as points inside the diamond polytope. There, it can be observed that most design variables have converged to the vertices of the polytope. Notably, a large number of variables that point to iron lie in the vicinity of the vertex. Indeed, at high flux densities, intermediate materials may carry more flux than iron because of penalization, which is analyzed in detail in Section 4.3.

Regarding the optimized design, one can identify small design features where portions of materials appear isolated from the main bulk. Fig. 14 decomposes the topology by material to facilitate the visualization of these zones. According to our numerical experiments, these small design features are caused by a poor convergence of the optimization problem to a local optimum and not by numerical instabilities such as a checkerboard. This can be seen in Figure 15, where two results obtained with the same set of parameters but with different discretization (coarse and refined) are presented. Both topologies are the same, i.e., the global shape and arrangement of the materials are the same. Similar to Choi and Yoo [47], neither checkerboard nor mesh-dependence was found, so no filtering process was used for the rest of the numerical experiments. This could be the subject of future work, such as when incorporating manufacturing constraints.

The optimized design in Fig. 12c contains three conductor slots, while the reference design contains six slots. The topology change between the reference and the optimized structures demonstrates the

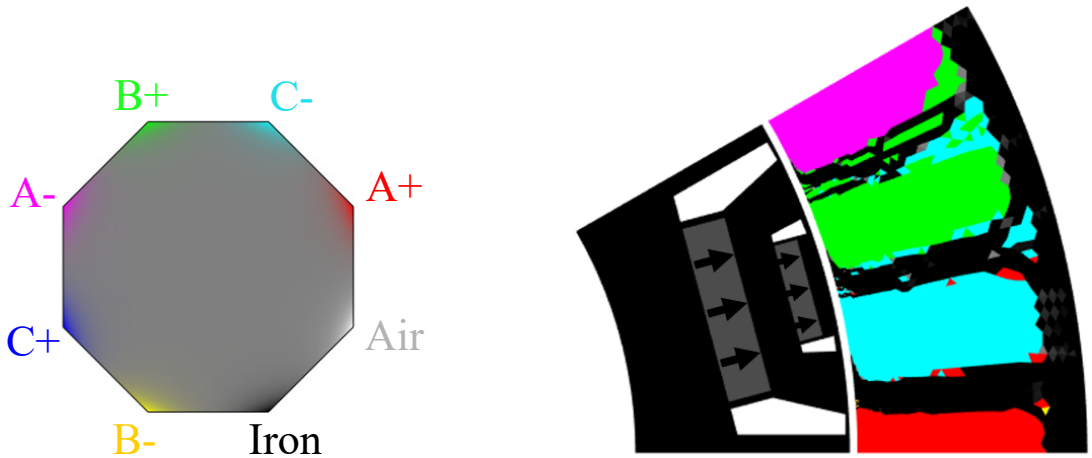

(a) Octagon

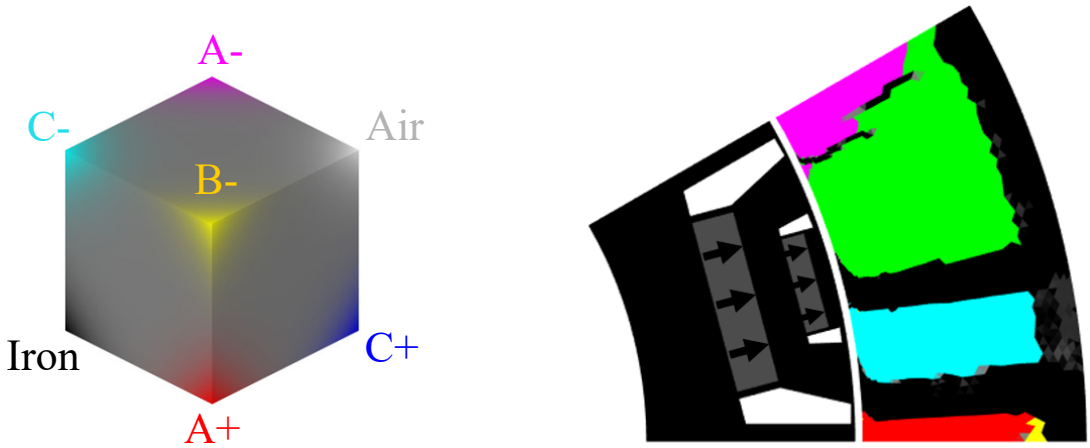

(b) Cube (representative of the literature)

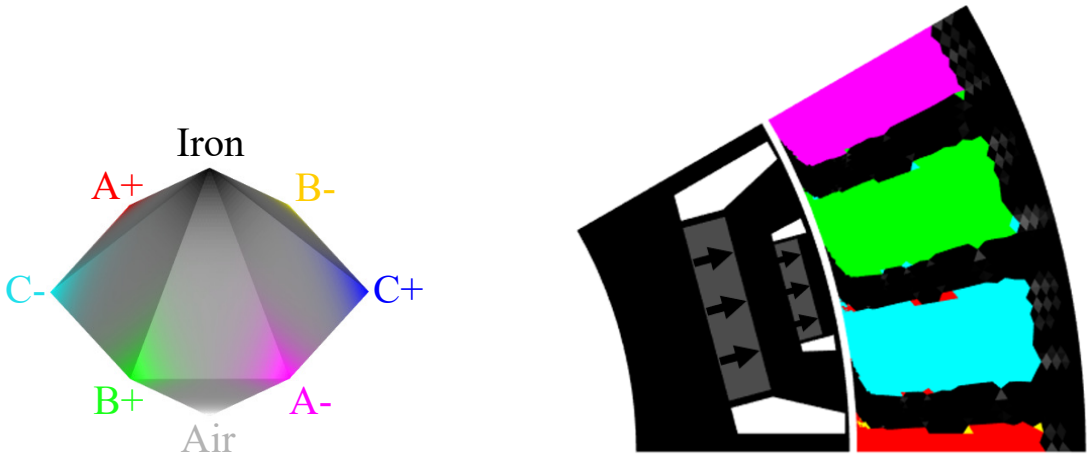

(c) Diamond

Figure 12: Different interpolation domains associated with their final design.

usefulness of a MMTO, as the optimized design is unreachable with parametric or shape optimization approaches. However, the numerical results given in Table 3 indicates that the cube (Fig. 12b) returns a structure associated with higher torque. These obtained structures are then fed with currents with

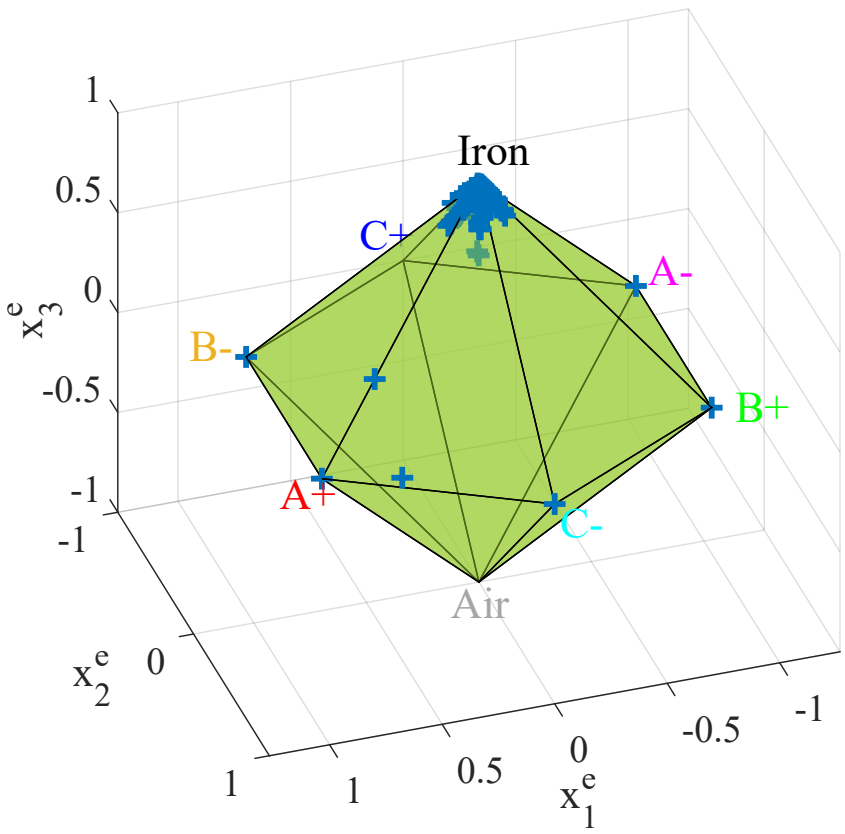

Figure 13: Repartition of the optimization variables for the design plotted in Fig. 12c. Each point represents the material of a mesh element from the stator.

different load angles ψ, as for a real machine where the optimal feeding is determined from its design. The resulting torques plotted in Fig. 17 show clearly that the diamond gives a structure that can reach higher torque than the two other designs, and even higher than the reference machine. Therefore, the structure obtained with a diamond-based catalog is better than the two others, as ψ represents only a rotation between the same stator and the rotor. Moreover, it seems closer to convergence than the other domains as the relative variation of the objective function is 1000 times lower, as shown in the 4th row of Table 3. Note that when the step size becomes too big, some iterations may be rejected by Algorithm 1, so Table 3 also gives the number of accepted iterations. For the rest of the numerical experiments, we thus choose to use the diamond domain. Note that a diamond-type domain can be used with this approach to address stator configurations that have a number of materials other than 8, as shown in Fig. 16.

Table 3: Optimization results with different domains.

Domains	**Octagon**	**Cube**	**Diamond**
Torque (Nm/m)	1703	1836	1720
Total iter.	500	500	500
Accepted iter.	401	400	395
$\frac{\lvert f_{\text{end}} - f_{\text{end}-1}\rvert}{f_{\text{end}}}$	2.0×10^{-5}	2.3×10^{-5}	3.4×10^{-8}

Nevertheless, Fig. 17 shows that the load angle where the torque is maximum ψ_{max} is shifted from the angle ψ_{optim} imposed during the optimization process. It means that a simple rotation applied to

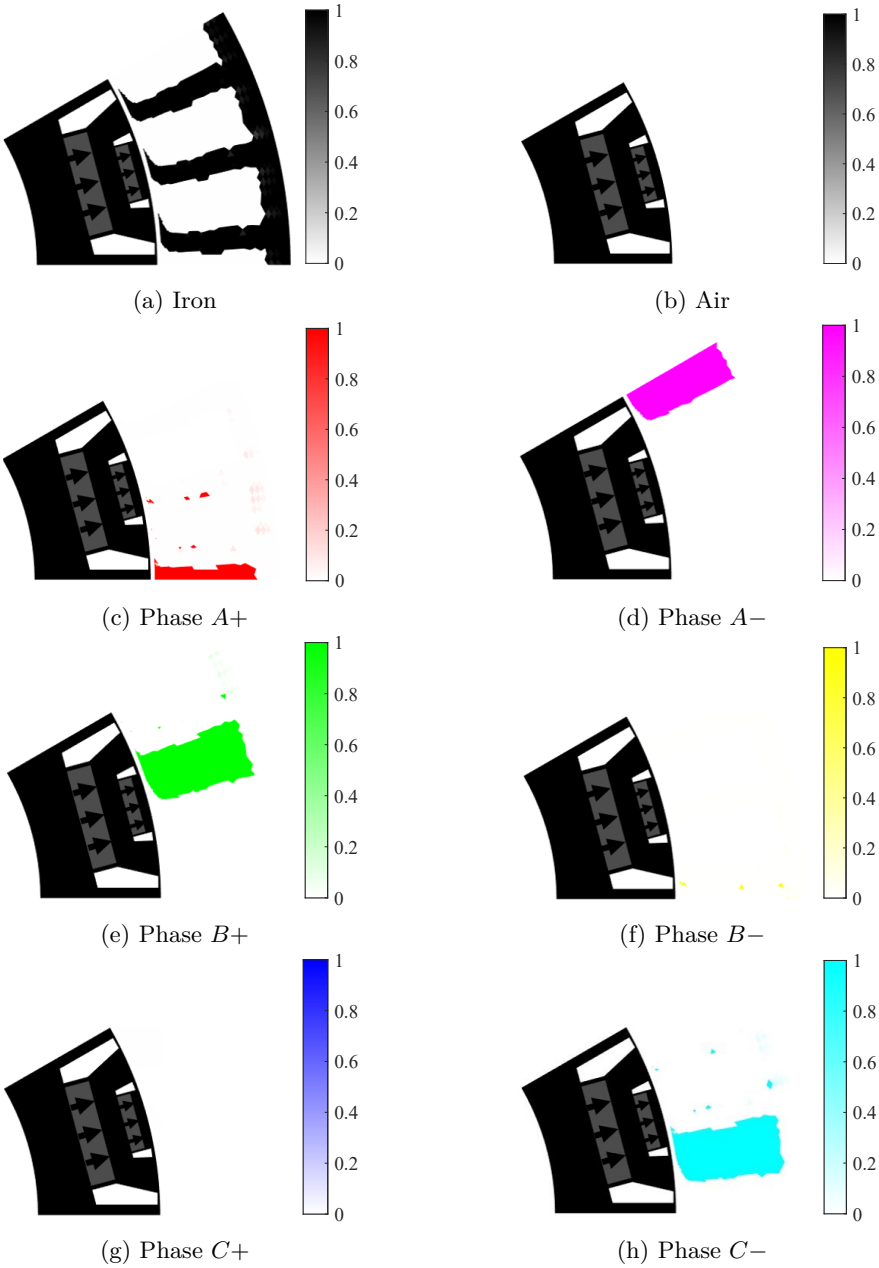

(a) Iron (b) Air (c) Phase $A+$ (d) Phase $A-$ (e) Phase $B+$ (f) Phase $B-$ (g) Phase $C+$ (h) Phase $C-$

Figure 14: Decomposition of the spatial distribution of each material of the design represented in Fig. 12c

the obtained structure gives a better torque; that is to say, the results are stuck in *local optima*. Possible causes and a solution to this problem are analyzed in Section 4.4.

4.3 Penalization parameter

Once the domain and materials placement are chosen, which are global and apply to all physical properties, the choice of the penalization is tricky. There are two material coefficients to interpolate in the partial differential equation (2): the magnetic reluctivity ν and the current density j. The associated penalization coefficients are p_ν and p_j, respectively. Their role is to avoid intermediate materials to have interesting properties simultaneously (*i.e.* high current density and good magnetic property). In this

(a) Coarse mesh (5935 triangles, 3126 nodes)

(b) Fine mesh (29833 triangles, 15268 nodes)

Figure 15: Optimized stator designs with a diamond domain and different meshes.

paper, we use the RAMP interpolation scheme proposed on Equation (17) directly on ν. While the obtained design does not seem sensitive to p_j, the ν-interpolation strongly influences the result, which should be investigated. Its value is tested between 0 (which corresponds to a linear interpolation) and 10. We found that for low p_ν values, the final designs tend to have very little steel, as shown in Fig 18b. The steel quantity in the stator teeth and the average torque increase with p_ν, until the steel is replaced by gray material for a high p_ν value, as shown in Fig. 18. The presence of intermediate materials in converged design can be explained because they carry a higher flux density $|\boldsymbol{b}|$ than the steel for high magnetic field $|\boldsymbol{h}|$. Indeed, the physical limit of a ferromagnetic material's reluctivity is:

$$\lim_{|\boldsymbol{b}|\to\infty} \nu(|\boldsymbol{b}|) = \nu_0, \tag{19}$$

while the limit reluctivity $\tilde{\nu}$ of the interpolated materials with a strictly convex penalization scheme such as (17) with $p_\nu > 0$ is:

$$\lim_{|\boldsymbol{b}|\to\infty} \tilde{\nu}(\mathbf{x}^e, |\boldsymbol{b}|) = \nu_0 \sum_{v=1}^{M} P(\omega_v^{\mathcal{D}}(\mathbf{x}^e)) < \nu_0. \tag{20}$$

Therefore, intermediate materials can carry more flux than steel and are *better* magnetic materials than steel for high flux densities $|\boldsymbol{b}|$, which justifies their existence in the converged designs. In practice, the larger p, the lower the $|\boldsymbol{b}|$ limit under which the steel is better than intermediate materials. To quantify the presence of intermediate materials, we use the following discreteness indicator in the optimization zone:

$$D(\mathbf{x}) = \frac{\displaystyle\sum_{e=1}^{N} \left[V_e \sum_{v=1}^{M} P(\omega_v(\mathbf{x}^e)) - P(\omega_v(\mathbf{x}_0)) \right]}{\displaystyle\sum_{e=1}^{N} V_e \left[1 - \sum_{v=1}^{M} P(\omega_v(\mathbf{x}_0)) \right]}, \tag{21}$$

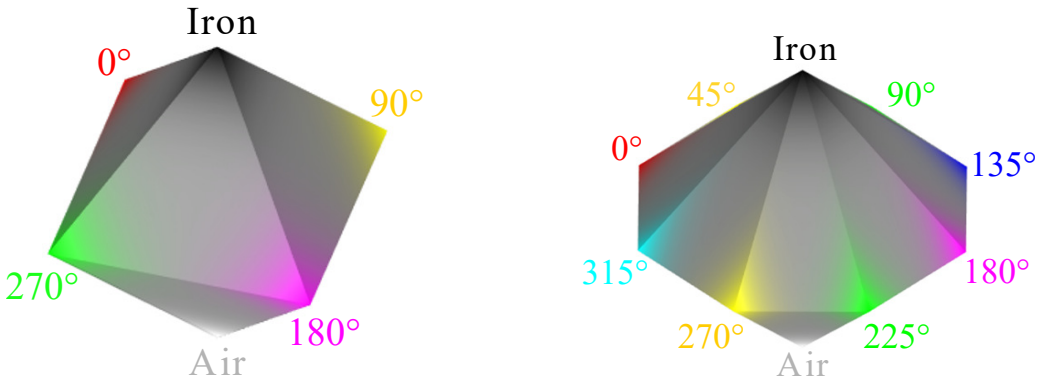

(a) 2 phases (6 materials) (b) 4 phases (10 materials)

Figure 16: Examples of diamond-type domains as in Fig. 12c for other multiphased stator. The numbers indicate the electric phases.

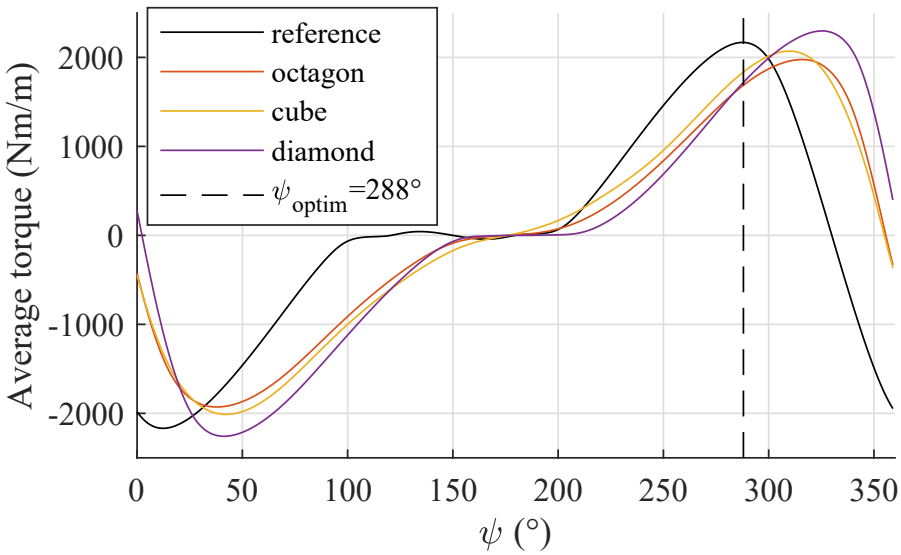

Figure 17: Evolution of the average torque of optimized structures with the load angle ψ.

with ω_v the Wachspress basis function verifying the partition of unity, V_e the surface of the e-mesh element, and P a convex penalization function. Equation (21) is 0 when all the $\mathbf{x}^e$ are in the center $\mathbf{x}_0$ of $\mathcal{D}$, and 1 if they are all on its vertices (prescribed materials). We arbitrary chose Equation (17) with $p = 2$ for P in (21). A compromise must be made to get a realistic design with a high torque, as shown in Fig. 18a. The relative variations of the objective function becomes lower than 10^{-6} for all designs, which indicates gray materials exists in converged results for high p_ν. We chose $p_\nu = 4$ and $p_j = 3$ for the remaining numerical tests, which gives good performances with a discreteness around 0.99.

4.4 Discussion on the local optima issue

As shown in Fig. 17, the average torque is not maximum at $\psi = \psi_{\text{optim}} = 288°$. The situation is illustrated in Fig. 19. The optimum load angle shift means that we can rotate the optimized structure, shown in Fig. 19a to obtain a *better* design, shown in Fig. 19b under the same electric conditions. Therefore the optimized design is necessarily a local optimum.

At least two causes may lead to local optima: the PM induced a field in the initial situation, which

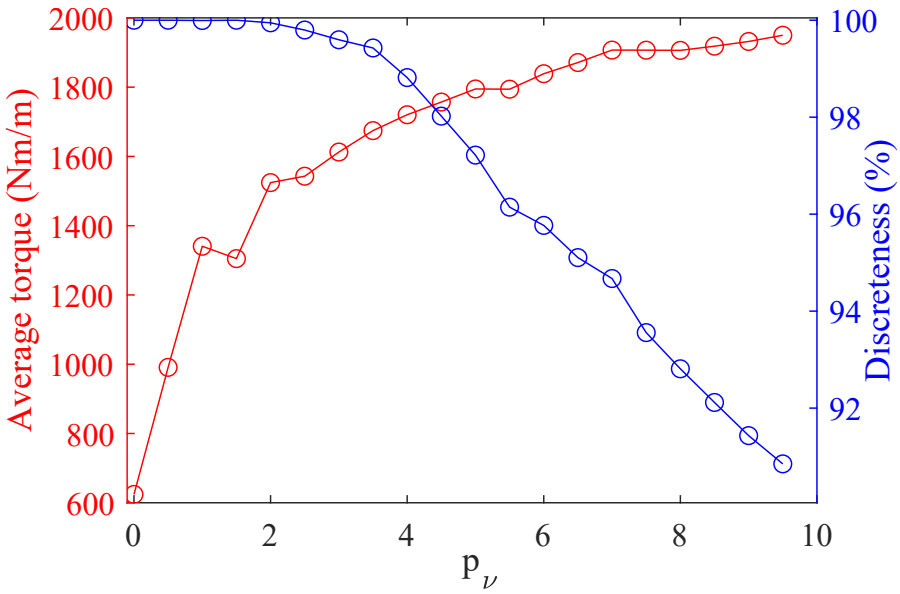

(a) Final torque and discreteness (21) with p_ν.

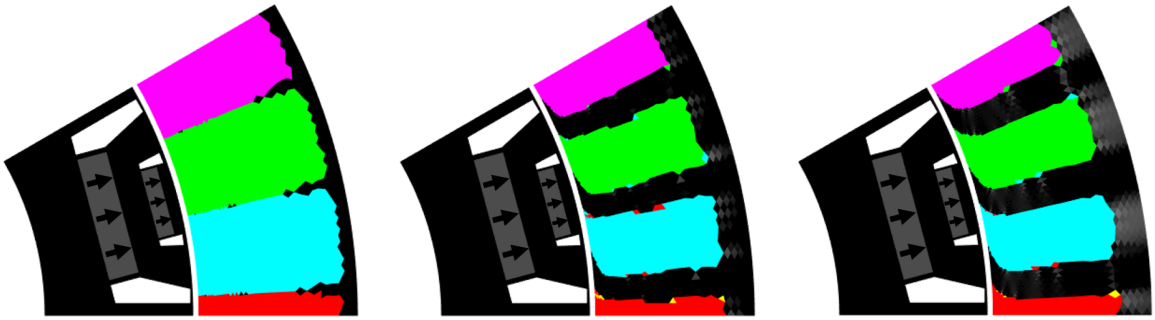

(b) $p_\nu = 0$ (c) $p_\nu = 4$ (d) $p_\nu = 8$

Figure 18: Effect of p_ν on the converged designs.

may lead the design variables in a bad direction, which is analyzed in Section 4.4.1, and the penalization plays a role as in the compliance problem, analyzed in Section 4.4.2. To avoid the algorithm being stuck in local optima, we propose in Section 4.4.3 to adjust ψ with a parametric optimization performed all the n_ψ iteration of the main algorithm independently.

4.4.1 Influence of the remanence

Only two different components can produce a non-zero average torque. The hybrid component is due to the interaction between the winding flux and the magnet flux, while the reluctant component is due to the non-uniformity of the magnetic flux paths.

The initial situation is a uniform material with no current. The only magnetic flux comes from the permanent magnets, which may promote too much the hybrid torque against the reluctant one at the beginning of the optimization process. This may lead to the shift between ψ_{optim} and $\psi_{\max}$ shown in Fig. 17.

This influence can be verified numerically by removing the permanent magnet remanence B_r from the optimization, so the concurrence between the two torque components vanishes. In practice, it is impossible to start the optimization with no source because the physical field $\boldsymbol{a}$ is null, and so are the sensitivities – see Equation (9). Therefore, we started with $B_r = 1\,\mu\text{T}$. The influence of B_r on the final

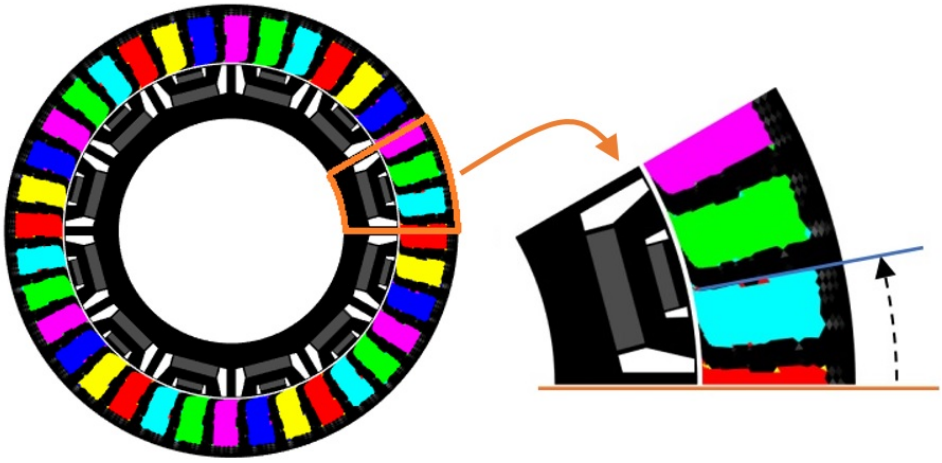

(a) Obtained design with a load angle shift (local optimum).

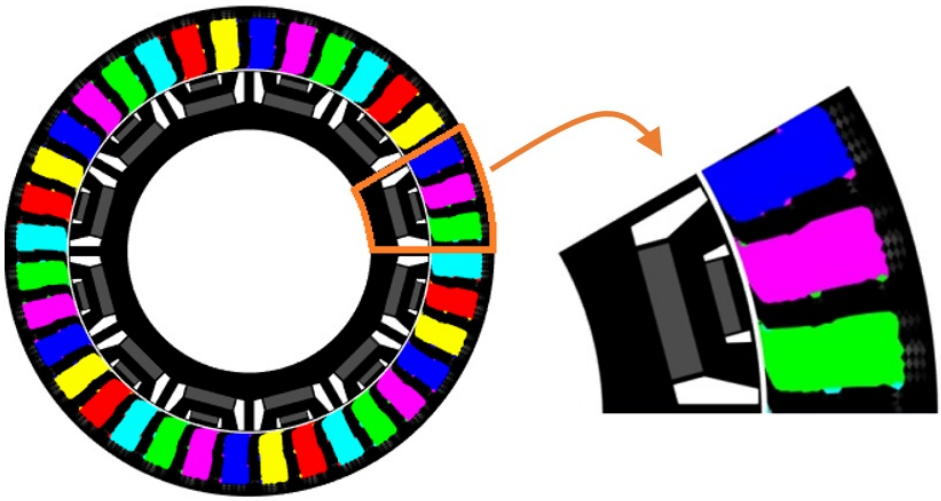

(b) Potential global optimum (no load angle shift).

Figure 19: Illustration of the effect of the load angle shift on the design.

design is plotted in Fig. 20. We note that the bigger the remanence, the bigger the shift between $\psi_{\max}$ and ψ_{optim}, which highlights the role of B_r in getting local optima.

4.4.2 Influence of the penalization

Another difficulty for avoiding local optima is the penalization. It is known that for simple problems, such as compliance minimization, a penalized material interpolation function breaks the convexity of the problem [59].

To illustrate the non-convexity induced by the penalization, we use the following procedure. The penalization parameters of the magnetic reluctivity (p_ν) and the current density (p_j) are initialized as $p_\nu = 4$ and $p_j = 3$. After 20 iterations, the design is almost converged and similar to Fig. 12c, which is a local optimum, so the penalization is removed by setting $p_\nu = 0$ and $p_j = 0$. Next, 10 more iterations are carried out, then the penalization of the current density is reactivated as $p_j = 3$ to remove intermediate materials, and the optimization problem is run until convergence. The average torque and some intermediate designs during optimization are plotted in Fig. 22 and 23, respectively.

Fig. 23 shows that during the optimization process, materials that were committed for a specific penalization can be decommitted and associated to another material when the penalization is changed.

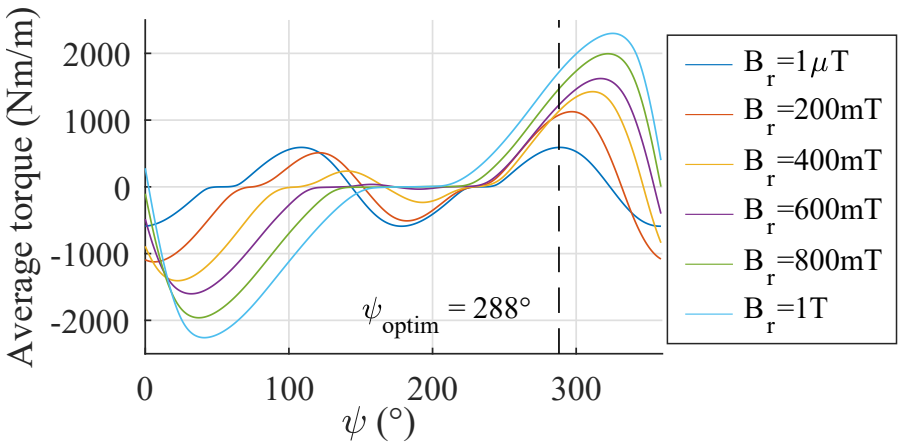

(a) Evolution of the torque with ψ.

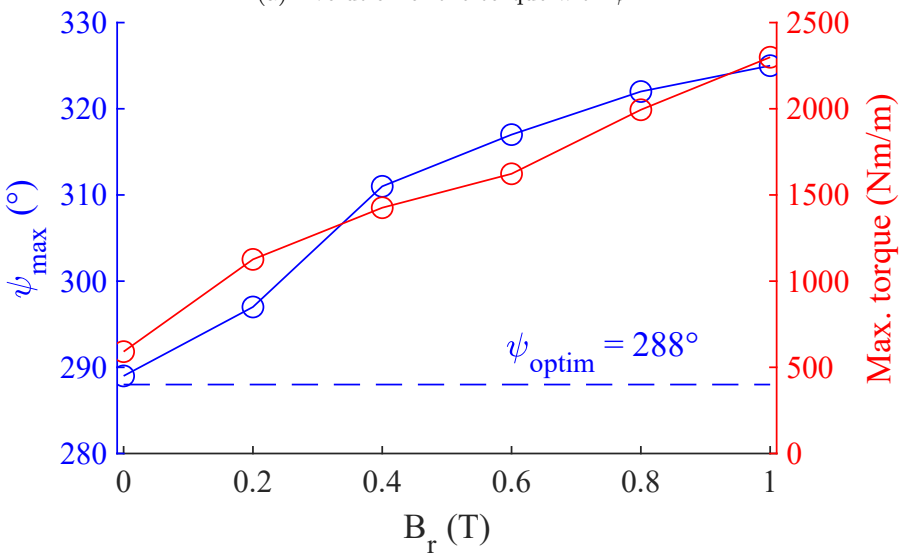

(b) $\psi_{\max}$ and its associated torque.

Figure 20: Torque of optimized designs and load angle ψ for different remanences B_r.

It can also be observed that such a scheme presents in its final design a smaller number of isolated materials (material zones that are represented by only one element) compared to the designs obtained with a fixed penalization.

Regarding the performance, Fig. 23 shows that the final design artificially changes the magnetic phase by mixing some electrical phases within a single slot instead of mechanically rotating the whole structure. By doing so, the load angle shift is highly reduced, as shown in Fig. 24, and the torque is increased. This result confirms that the penalization leads to a local optimum shown in Fig. 23c, and the modification of the penalization parameters allows to get better designs such as the structure shown in Fig. 23f.

4.4.3 Parametric ψ adjustement

The shift between the optimization load angle ψ_{optim} and the maximum torque load angle $\psi_{\max}$ is an indicator of local optimum. A simple way to avoid this problem is to control ψ_{optim} to ensure that it is always equal to $\psi_{\max}$ with a parametric study. To save computation time, we can update ψ all the n_ψ iterations with Algorithm 2. $n_\psi = 1$ means ψ is ajusted every iterations, $n_\psi = \infty$ means it is never adjusted.

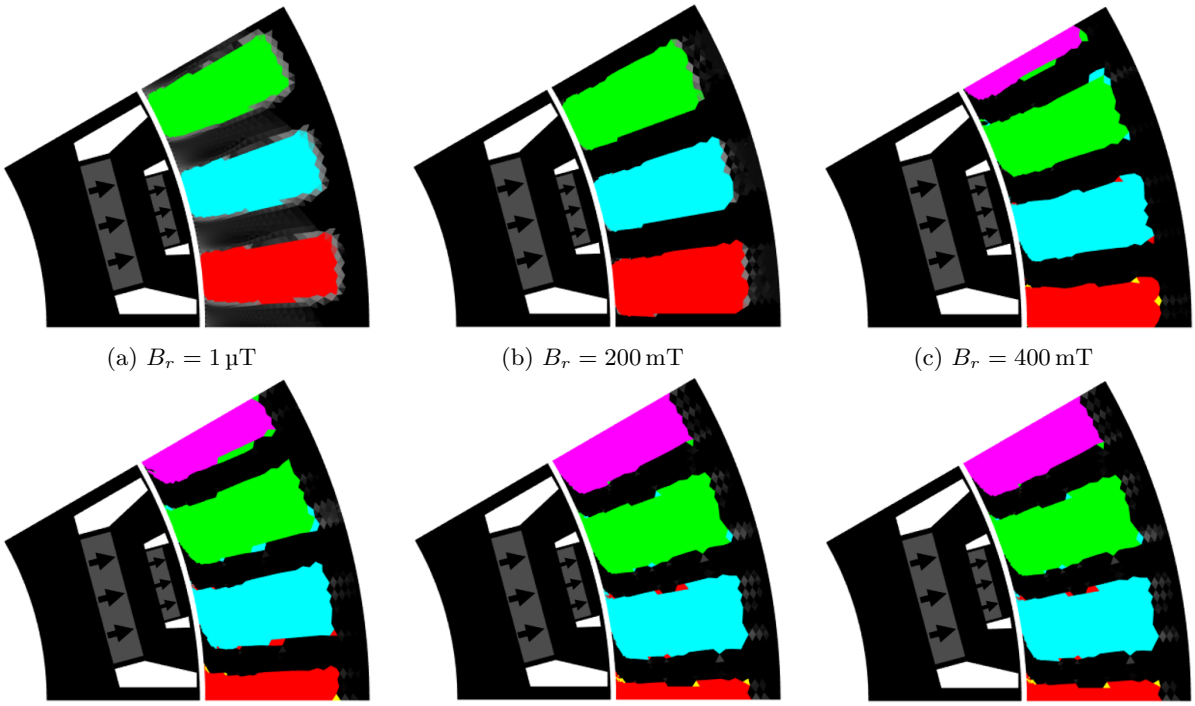

(a) $B_r = 1\,\mu\text{T}$ (b) $B_r = 200\,\text{mT}$ (c) $B_r = 400\,\text{mT}$

(d) $B_r = 600\,\text{mT}$ (e) $B_r = 800\,\text{mT}$ (f) $B_r = 1\,\text{T}$

Figure 21: Final designs obtained for different remanences.

This method was tested for several n_ψ. The results are given in Fig. 25 and the structures are shown in Fig. 26. The initial ψ value is $\psi_0 = 288°$. As expected, the more often ψ_0 is adjusted, the higher the torque. Moreover, the maximum torque with ψ adjustment is significantly higher than the maximum torque without, even with a high n_ψ value.

Algorithm 2 Control of ψ

Require: k, $\mathbf{x}_k$, n_ψ ▷ k is the number of the current iteration of the optimizer.
1: **if** modulo$(n_\psi, k) = 0$ **then**
2: **for** each $\psi_i \in [\![0°, 359°]\!]$ **do**
3: Compute $\langle T_i(\mathbf{x}_k)\rangle$ with $\psi = \psi_i$
4: Store $\langle T_i(\mathbf{x}_k)\rangle$ and ψ_i
5: **end for**
6: Find the max. torque and associated $\psi_{\max}$
7: $\psi \Leftarrow \psi_{\max}$
8: **end if**
9: Continue the optimization

Concerning the load angle, $\psi_{\max}$ drifts more from the initial ψ when n_ψ is small. Concerning the obtained structures, the final designs become more *symmetric* with frequent ψ adjustments, which indicates that *the asymmetry is also a local optimum.* The existence of this local optimum may be due to the PM flux as Fig. 21 seems to show a correlation between symmetry and remanence.

Moreover, low n_ψ gives "cleaner" designs, as all elements are the same conductor in a same slot for $n_\psi = 1$ and $n_\psi = 5$: the number of isolated islands of materials decreases with the frequency of the load angle adjustment. Therefore, we recommend adjusting ψ during the optimization process to avoid local optima. The computing time in Algorithm 2 can be reduced by considering a smaller angle interval

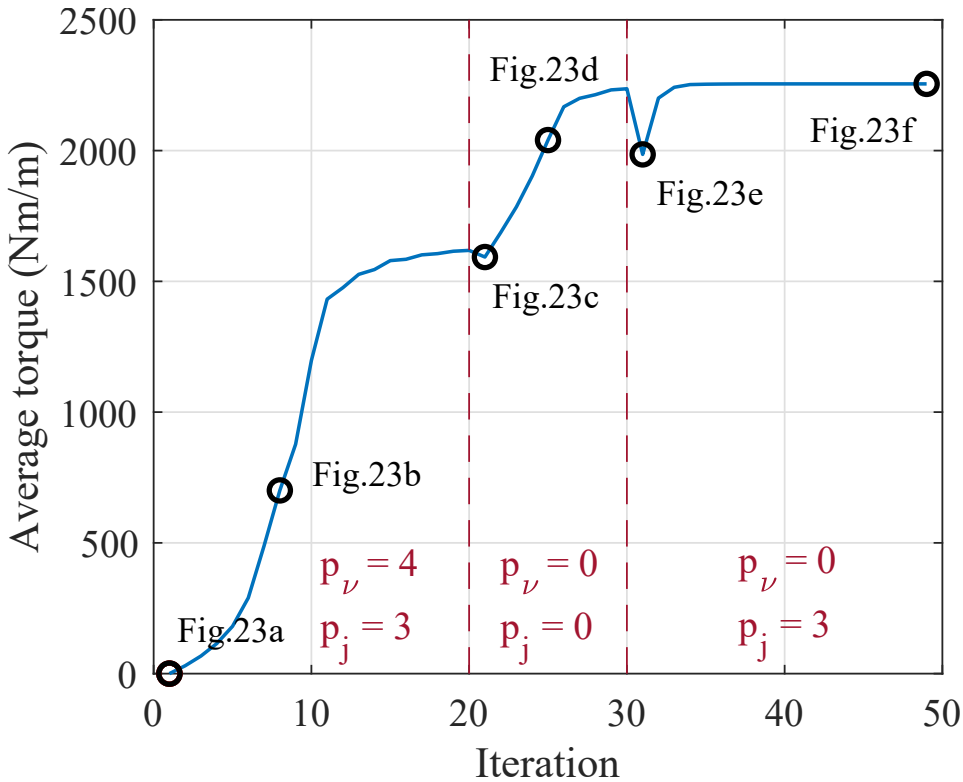

Figure 22: Average torque during topology optimization with penalization changes. The prescribed penalization is shown in red.

centered on the current ψ_i in the parametric study.

5 Conclusion

This paper presented a general density-based topology optimization methodology designed to support many different materials. It extends the SFP scheme to non-orthogonal interpolation domains using Wachspress basis functions with a projected gradient algorithm. We applied this methodology to the challenging 8-materials optimization of a 3-phase PMSM stator. Performing and meaningful designs were obtained, demonstrating this methodology's potential. In addition, we highlighted the importance and difficulties of choosing both a suitable interpolation domain and an appropriate material penalization to obtain satisfactory designs through numerical examples. We show that classic orthogonal domains are not suitable for all MMTO problems. In fact, a diamond domain appears to be better suited for this application and may also apply to a different number of electric phases.

However, with a load-angle analysis, we found that this methodology could return local optima, as in all gradient-based optimization methods. In this application, they are caused at least by the presence of an external field source – identified as the permanent magnets – and the penalization of the material properties. Adjusting the load angle during optimization solves this issue and leads to better designs, transitioning from asymmetric to almost symmetric structures.

This methodology can be improved by adding global constraints to address industrial problems. For instance, imposing the conductors' volume associated with a given current density is directly related to controlling the total electric current. A solution is to use popular optimizers such as MMA or GCMMA [60]. It requires including the projection algorithm within the optimizer, which will be done in future work. This methodology could then be applied to other physics and objective functions. As this work

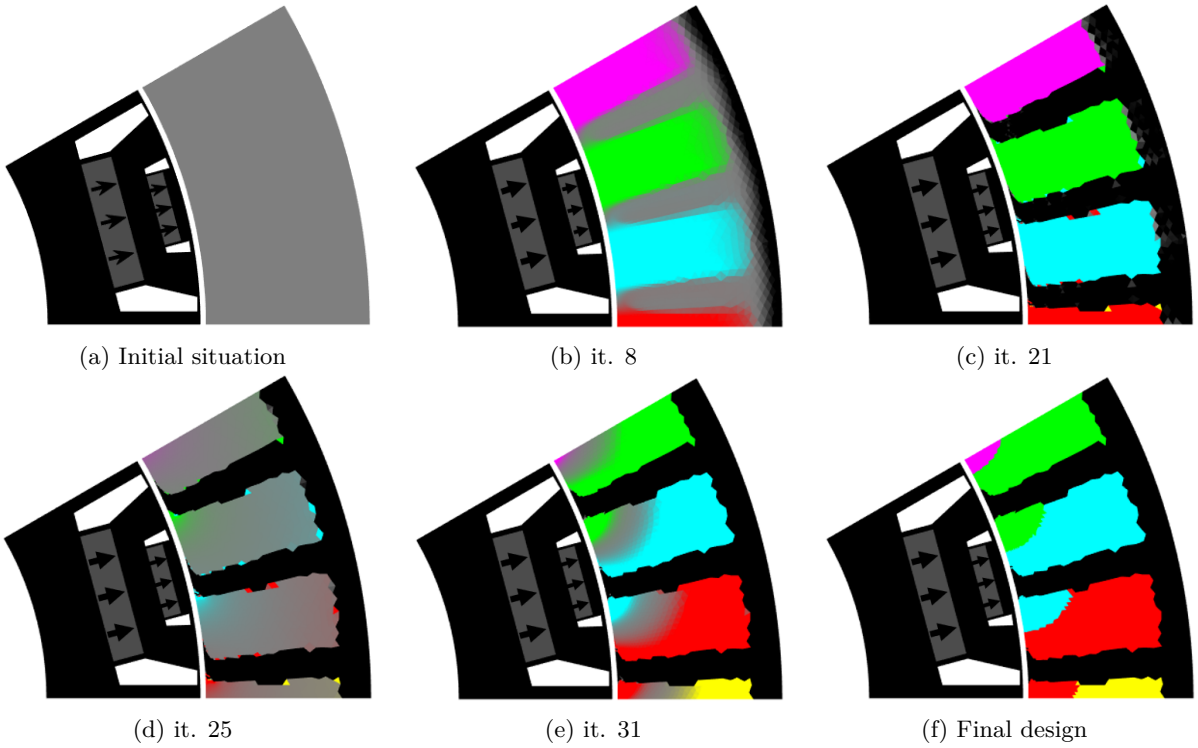

(a) Initial situation (b) it. 8 (c) it. 21

(d) it. 25 (e) it. 31 (f) Final design

Figure 23: Design snapshots during the optimization process with penalization changes. The average torque for each figure is illustrated in Fig. 22.

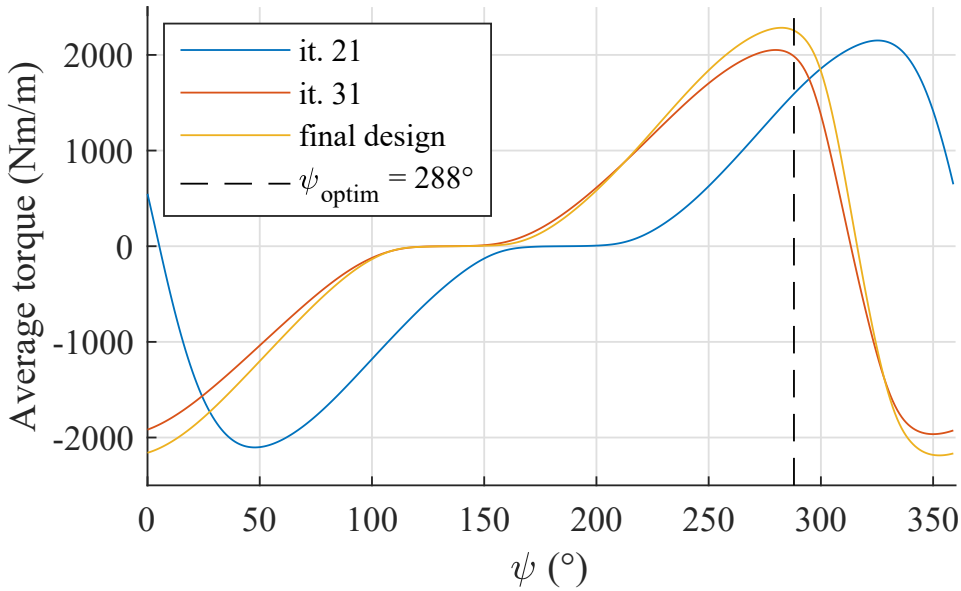

Figure 24: Evolution of the average torque with ψ at different steps of the penalization-change process.

extends the SFP scheme designed for composite materials in mechanical engineering, it could be used to optimize different fiber orientations, similar to the different electric phases within a PMSM.

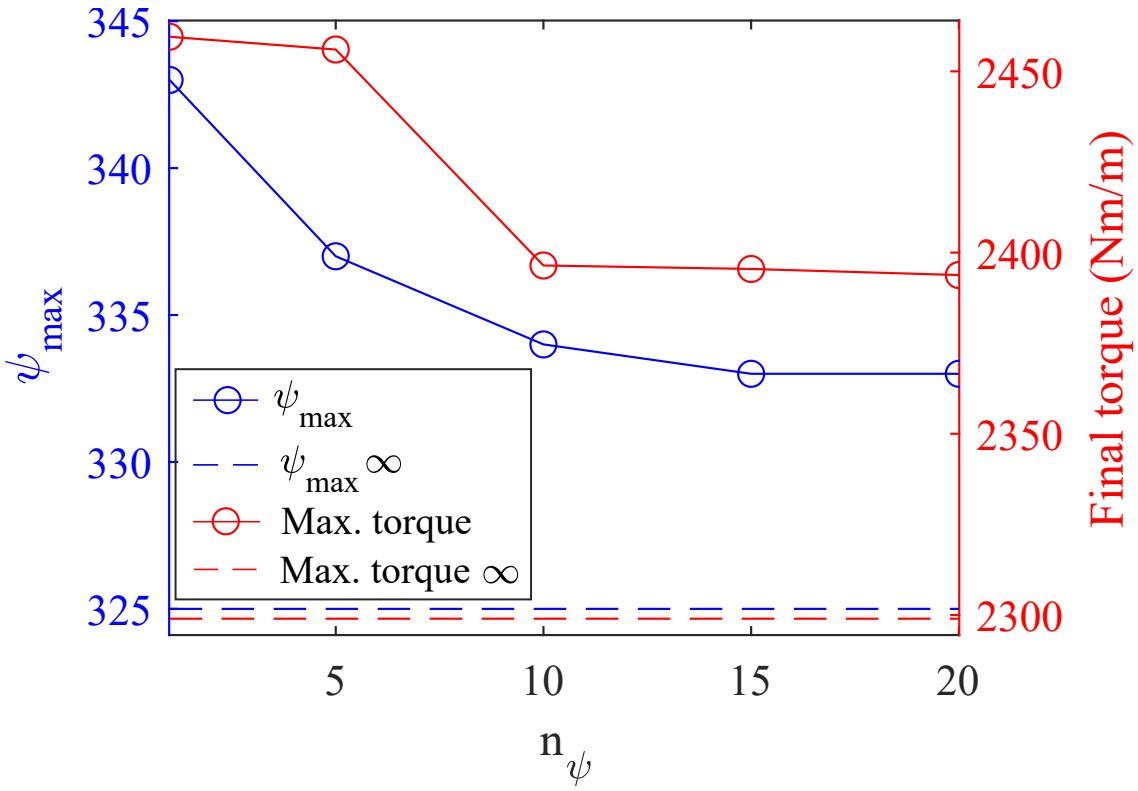

Figure 25: Final torque and $\psi_{\max}$ evolution with n_ψ.

Conflict of interest

On behalf of all authors, the corresponding author states that there is no conflict of interest.

Replication of results

Our work relies on the Matlab R2020b programming language. An implementation of the projection algorithm presented in Section 2 and the Wachspress interpolants computation presented in Section 3 are freely available on GitHub [52].

All other information required to replicate the results of this work is clearly detailed in the manuscript. The model, as well as the optimization algorithm, are given in Section 2. Interested readers may send a request to the corresponding author to obtain the .mat files of results.

References

[1] M. P. Bendsøe and N. Kikuchi. "Generating optimal topologies in structural design using a homogenization method." In: *Computer Methods in Applied Mechanics and Engineering* 71.2 (1988), pp. 197–224. DOI: 10.1016/0045-7825(88)90086-2 (cit. on p. 2).

[2] N. Aage, E. Andreassen, and B. S. Lazarov. "Topology optimization using PETSc: An easy-to-use, fully parallel, open source topology optimization framework." In: *Structural and Multidisciplinary Optimization* 51.3 (2015), pp. 565–572. DOI: 10.1007/s00158-014-1157-0 (cit. on p. 2).

[3] M. P. Bendsøe et al. "Topology optimization - Broadening the areas of application." In: *Control and Cybernetics* 34.1 (2005), pp. 7–36 (cit. on p. 2).

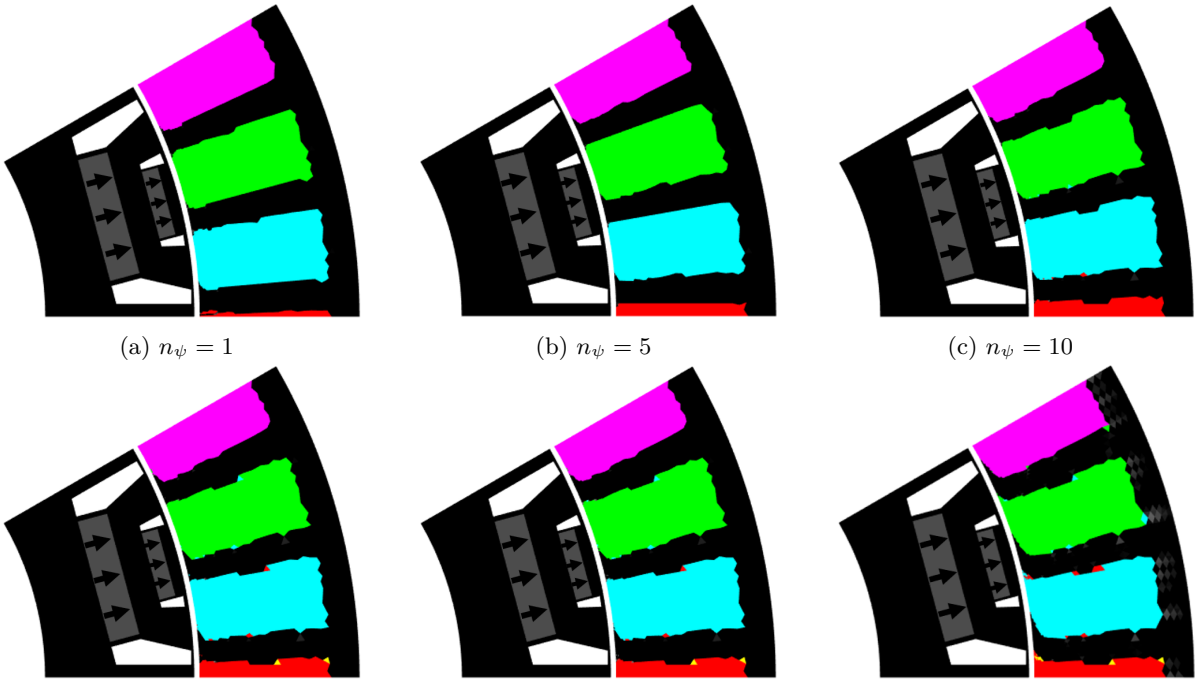

(a) $n_\psi = 1$ (b) $n_\psi = 5$ (c) $n_\psi = 10$

(d) $n_\psi = 15$ (e) $n_\psi = 20$ (f) $n_\psi = \infty$

Figure 26: Final designs obtained with different n_ψ values.

[4] O. Sigmund and K. Maute. "Topology optimization approaches." In: *Structural and Multidisciplinary Optimization* 48.6 (2013), pp. 1031–1055. DOI: 10.1007/s00158-013-0978-6 (cit. on p. 2).

[5] M. P. Bendsøe. "Optimal shape design as a material distribution problem." In: *Structural optimization* 1.4 (1989), pp. 193–202. DOI: 10.1007/BF01650949 (cit. on pp. 2, 11).

[6] M. Stolpe and K. Svanberg. "An alternative interpolation scheme for minimum compliance topology optimization." In: *Structural and Multidisciplinary Optimization* 22.2 (2001), pp. 116–124. DOI: 10.1007/s001580100129 (cit. on pp. 2, 11).

[7] J. Thomsen. "Topology Optimization of Structures Composed of One or Two Materials." In: *Evaluation of Global Bearing Capacities of Structures* 115 (1993), pp. 237–254. DOI: 10.1007/978-3-7091-2752-0_8 (cit. on p. 2).

[8] A. T. Gaynor et al. "Multiple-material topology optimization of compliant mechanisms created via PolyJet three-dimensional printing." In: *Journal of Manufacturing Science and Engineering* 136.6 (2014). DOI: 10.1115/1.4028439 (cit. on p. 2).

[9] H. Kazemi, A. Vaziri, and J. A. Norato. "Multi-material topology optimization of lattice structures using geometry projection." In: *Computer Methods in Applied Mechanics and Engineering* 363 (2020), p. 112895. DOI: 10.1016/j.cma.2020.112895 (cit. on p. 2).

[10] A. Takezawa and M. Kobashi. "Design methodology for porous composites with tunable thermal expansion produced by multi-material topology optimization and additive manufacturing." In: *Composites Part B: Engineering* 131 (2017), pp. 21–29. DOI: 10.1016/j.compositesb.2017.07.054 (cit. on p. 2).

[11] Y. Jung, J. Lee, and S. Min. "Multi-material topology optimization considering joint stiffness using a two-step filtering approach." In: *Finite Elements in Analysis and Design* 197 (2021), p. 103635. DOI: 10.1016/j.finel.2021.103635 (cit. on p. 2).

[12] M. He et al. "Multi-material topology optimization of piezoelectric composite structures for energy harvesting." In: *Composite Structures* 265 (2021), p. 113783. DOI: 10.1016/j.compstruct.2021.113783 (cit. on p. 2).

[13] M. Y. Wang and X. Wang. ""Color" level sets: A multi-phase method for structural topology optimization with multiple materials." In: *Computer Methods in Applied Mechanics and Engineering* 193.6-8 (2004), pp. 469–496. DOI: 10.1016/j.cma.2003.10.008 (cit. on p. 2).

[14] G. Allaire et al. "Multi-phase structural optimization via a level set method." In: *ESAIM - Control, Optimisation and Calculus of Variations* 20.2 (2014), pp. 576–611. DOI: 10.1051/cocv/2013076 (cit. on p. 2).

[15] S. Zhou and M. Y. Wang. "Multimaterial structural topology optimization with a generalized Cahn-Hilliard model of multiphase transition." In: *Structural and Multidisciplinary Optimization* 33.2 (2007), pp. 89–111. DOI: 10.1007/s00158-006-0035-9 (cit. on p. 2).

[16] R. Tavakoli. "Multimaterial topology optimization by volume constrained Allen-Cahn system and regularized projected steepest descent method." In: *Computer Methods in Applied Mechanics and Engineering* 276 (2014), pp. 534–565. DOI: 10.1016/j.cma.2014.04.005 (cit. on p. 3).

[17] R. Tavakoli and S. M. Mohseni. "Alternating active-phase algorithm for multimaterial topology optimization problems: A 115-line MATLAB implementation." In: *Structural and Multidisciplinary Optimization* 49.4 (2014), pp. 621–642. DOI: 10.1007/s00158-013-0999-1 (cit. on p. 3).

[18] A. Chandrasekhar and K. Suresh. "Multi-Material Topology Optimization Using Neural Networks." In: *CAD Computer Aided Design* 136 (2021), p. 103017. DOI: 10.1016/j.cad.2021.103017 (cit. on p. 3).

[19] D. N. Dyck and D. A. Lowther. "Automated design of magnetic devices by optimizing material distribution." In: *IEEE Transactions on Magnetics* 32.3 (1996), pp. 1188–1193. DOI: 10.1109/20.497456 (cit. on p. 3).

[20] S. Wang, S. Park, and J. Kang. "Multi-domain topology optimization of electromagnetic systems." In: *COMPEL - The International Journal for Computation and Mathematics in Electrical and Electronic Engineering* 23.4 (2004), pp. 1036–1044. DOI: 10.1108/03321640410553463 (cit. on p. 3).

[21] S. Wang et al. "Topology optimization of electromagnetic systems considering magnetization direction." In: *IEEE Transactions on Magnetics* 41.5 (2005), pp. 1808–1811. DOI: 10.1109/TMAG.2005.846480 (cit. on p. 3).

[22] J. S. Choi et al. "Optimization of magnetization directions in a 3-D magnetic structure." In: *IEEE Transactions on Magnetics* 46.6 (2010), pp. 1603–1606. DOI: 10.1109/TMAG.2010.2040251 (cit. on p. 3).

[23] J. Lee et al. "Topology optimization for three-dimensional design of segmented permanent magnet arrays." In: *Structural and Multidisciplinary Optimization* 62.6 (2020), pp. 3089–3104. DOI: 10.1007/s00158-020-02656-7 (cit. on p. 3).

[24] J. Lee, E. M. Dede, and T. Nomura. "Simultaneous Design Optimization of Permanent Magnet, Coils, and Ferromagnetic Material in Actuators." In: *IEEE Transactions on Magnetics* 47.12 (2011), pp. 4712–4716. DOI: 10.1109/TMAG.2011.2160870 (cit. on p. 3).

[25] J. Lee et al. "Multi-material topology optimization of magnetic actuator with segmented permanent magnets." In: *IEEE Transactions on Magnetics* 54.7 (2018), pp. 1–6. DOI: 10.1109/TMAG.2018.2824287 (cit. on p. 3).

[26] T. Jung, J. Lee, and J. Lee. "Design and Fabrication of Magnetic System Using Multi-Material Topology Optimization." In: *IEEE Access* 9 (2021), pp. 8649–8658. DOI: 10.1109/ACCESS.2021.3049271 (cit. on p. 3).

[27] T. Sato, K. Watanabe, and H. Igarashi. "Multimaterial topology optimization of electric machines based on normalized Gaussian network." In: *IEEE Transactions on Magnetics* 51.3 (2015), pp. 3–6. DOI: 10.1109/TMAG.2014.2359972 (cit. on p. 3).

[28] S. W. Jung, J. S. Ro, and H. K. Jung. "A Hybrid Algorithm Using Shape and Topology Optimization for the Design of Electric Machines." In: *IEEE Transactions on Magnetics* 54.3 (2018), pp. 2018–2021. DOI: 10.1109/TMAG.2017.2764753 (cit. on p. 3).

[29] F. Guo et al. "Multimaterial Magneto-Structural Topology Optimization of Wound Field Synchronous Machine Rotors." In: *IEEE Transactions on Industry Applications* 56.4 (2020), pp. 3656–3667. DOI: 10.1109/TIA.2020.2989682 (cit. on p. 3).

[30] T. Gauthey, P. Gangl, and M. Hage Hassan. *Multi-Material Topology Optimization with Continuous Magnetization Direction for Permanent Magnet Synchronous Reluctance Motors.* 2021. DOI: 10.48550/ARXIV.2107.04825 (cit. on p. 3).

[31] C. Lee and I. Gwun. "Multi - material topology optimization for the PMSMs under the consideration of the MTPA control." In: *Structural and Multidisciplinary Optimization* (2022), pp. 1–11. DOI: 10.1007/s00158-022-03367-x (cit. on p. 3).

[32] S. Park, J. Lee, and J. Lee. "Multi-material topology optimization of permanent magnet synchronous motors." In: *International Journal of Applied Electromagnetics and Mechanics* 67.4 (2021), pp. 461–472. DOI: 10.3233/JAE-210062 (cit. on p. 3).

[33] E. Kuci et al. "Combination of topology optimization and Lie derivative-based shape optimization for electro-mechanical design." In: *Structural and Multidisciplinary Optimization* 59.5 (2019), pp. 1723–1731. DOI: 10.1007/s00158-018-2157-2 (cit. on p. 3).

[34] J. Lee, J. H. Seo, and N. Kikuchi. "Topology optimization of switched reluctance motors for the desired torque profile." In: *Structural and Multidisciplinary Optimization* 42.5 (2010), pp. 783–796. DOI: 10.1007/s00158-010-0547-1 (cit. on pp. 3, 12).

[35] J. S. Choi et al. "Topology optimization of the stator for minimizing cogging torque of IPM motors." In: *IEEE Transactions on Magnetics* 47.10 (2011), pp. 3024–3027. DOI: 10.1109/TMAG.2011.2158572 (cit. on pp. 3, 12).

[36] T. Labbé and B. Dehez. "Convexity-Oriented Mapping Method for the Topology Optimization of Electromagnetic Devices Composed of Iron and Coils." In: *IEEE Transactions on Magnetics* 46.5 (2010), pp. 1177–1185. DOI: 10.1109/CEFC.2010.5481713 (cit. on pp. 3, 12).

[37] M. P. Bendsøe and O. Sigmund. *Topology optimization: theory, methods, and applications.* Springer Berlin, Heidelberg, 2003, p. 120. DOI: 10.1007/978-3-662-05086-6 (cit. on p. 3).

[38] L. Yin and G. Ananthasuresh. "Topology optimization of compliant mechanisms with multiple materials using a peak function material interpolation scheme." In: *Structural and Multidisciplinary Optimization* 23.1 (2001), pp. 49–62. DOI: 10.1007/s00158-001-0165-z (cit. on p. 3).

[39] W. Zuo and K. Saitou. "Multi-material topology optimization using ordered SIMP interpolation." In: *Structural and Multidisciplinary Optimization* 55.2 (2017), pp. 477–491. DOI: 10.1007/s00158-016-1513-3 (cit. on p. 3).

[40] E. Lund, L. Kuhlmeier, and J. Stegmann. "Buckling optimization of laminated hybrid composite shell structures using discrete material optimization." In: *6th World Congress on Structural and Multidisciplinary Optimization.* Vol. 30. ISSMO. Rio de Janeiro, Brasil, 2005 (cit. on p. 3).

[41] M. Bruyneel. "SFP—a new parameterization based on shape functions for optimal material selection: application to conventional composite plies." In: *Structural and Multidisciplinary Optimization* 43.1 (2011), pp. 17–27. DOI: 10.1007/s00158-010-0548-0 (cit. on pp. 3, 9, 11).

[42] M. Bruyneel et al. "Extensions of the shape functions with penalization parameterization for composite-ply optimization." In: *AIAA journal* 49.10 (2011), pp. 2325–2329. DOI: 10.2514/1.J051225 (cit. on pp. 3, 13).

[43] T. Gao, W. Zhang, and P. Duysinx. "A bi-value coding parameterization scheme for the discrete optimal orientation design of the composite laminate." In: *International Journal for Numerical Methods in Engineering* 91 (2012), pp. 98–114. DOI: 10.1002/nme.3279 (cit. on p. 3).

[44] X. S. Zhang, H. Chi, and Z. Zhao. "Topology optimization of hyperelastic structures with anisotropic fiber reinforcement under large deformations." In: *Computer Methods in Applied Mechanics and Engineering* 378 (2021), p. 113496. DOI: 10.1016/j.cma.2020.113496 (cit. on p. 3).

[45] O. Sigmund. "Design of multiphysics actuators using topology optimization - Part II: Two-material structures." In: *Computer Methods in Applied Mechanics and Engineering* 190.49-50 (2001), pp. 6577–6604. DOI: 10.1016/S0045-7825(01)00251-1 (cit. on p. 3).

[46] Y. Jung and S. Min. "Material Interpolation in Multi-Material Topology Optimization for Magnetic Device Design." In: *IEEE Transactions on Magnetics* 55.11 (2019), pp. 2019–2022. DOI: 10.1109/TMAG.2019.2929079 (cit. on pp. 3–4, 10).

[47] J. S. Choi and J. Yoo. "Simultaneous structural topology optimization of electromagnetic sources and ferromagnetic materials." In: *Computer Methods in Applied Mechanics and Engineering* 198.27-29 (2009), pp. 2111–2121. DOI: 10.1016/j.cma.2009.02.015 (cit. on pp. 3–4, 14).

[48] E. L. Wachspress. *A Finite Element Rational Basis*. Vol. 114. Mathematics in Science and Engineering. Academic Press, Inc., 1975. DOI: 10.1016/s0076-5392(09)60113-2 (cit. on pp. 3, 11).

[49] A. Arkkio. "Analysis of Induction Motors Based on the Numerical Solution of the Magnetic Field and Circuit Equations." PhD thesis. Helsinki University of Technology, 1987 (cit. on p. 5).

[50] E. Hinton, J. Sienz, and M. Özakça. *Analysis and optimization of Prismatic and Axisymetric Shell Structure*. Springer-Verlag, 2003, pp. 113–114. DOI: 10.1007/978-0-85729-424-1 (cit. on p. 6).

[51] J. Nocedal and S. J. Wright. *Numerical optimization*. Springer New York, NY, 2006, pp. 1–664. DOI: 10.1007/978-0-387-40065-5 (cit. on p. 6).

[52] T. Cherrière and L. Laurent. *Wachspress2D3D, v1.0.0*. 2022. DOI: 10.5281/zenodo.6630215 (cit. on pp. 8, 11, 26).

[53] N. Sukumar and E. A. Malsch. "Recent advances in the construction of polygonal finite element interpolants." In: *Archives of Computational Methods in Engineering* 13.1 (2006), pp. 129–163. DOI: 10.1007/BF02905933 (cit. on p. 11).

[54] M. Kraus, A. Rajagopal, and P. Steinmann. "Investigations on the polygonal finite element method: Constrained adaptive Delaunay tessellation and conformal interpolants." In: *Computers and Structures* 120.February (2013), pp. 33–46. DOI: 10.1016/j.compstruc.2013.01.017 (cit. on p. 11).

[55] M. Floater, A. Gillette, and N. Sukumar. "Gradient bounds for Wachspress coordinates on polytopes." In: *SIAM Journal on Numerical Analysis* 52.1 (2014), pp. 515–532. DOI: 10.1137/130925712 (cit. on p. 11).

[56] H. Sato and H. Igarashi. "Deep learning-based surrogate model for fast multi-material topology optimization of IPM motor." In: *COMPEL - The International Journal for Computation and Mathematics in Electrical and Electronic Engineering* 41.3 (2022), pp. 900–914. DOI: 10.1108/COMPEL-03-2021-0086 (cit. on p. 12).

[57] D. Staton and J. Goss. "Open Source Electric Motor Models for Commercial EV & Hybrid Traction Motors." In: *CWIEME*. Berlin, 2017, pp. 46–59 (cit. on pp. 12–13).

[58] C. Geuzaine and J. Remacle. "Gmsh: A 3-D finite element mesh generator with built-in pre- and post-processing facilities." In: *International Journal for Numerical Methods in Engineering* 79.May (2009), pp. 1309–1331. DOI: 10.1002/nme.2579 (cit. on p. 12).

[59] M. Abdelhamid and A. Czekanski. "Revisiting non-convexity in topology optimization of compliance minimization problems." In: *Engineering Computations (Swansea, Wales)* 39.3 (2022), pp. 893–915. DOI: 10.1108/EC-01-2021-0052 (cit. on p. 21).

[60] K. Svanberg. "A Class of Globally Convergent Optimization Methods Based on Conservative Convex Separable Approximations." In: *SIAM Journal on Optimization* 12.2 (2002), pp. 555–573. DOI: 10.1137/S1052623499362822 (cit. on p. 24).